Chemical Science

ROYAL SOCIETY OF CHEMISTRY

REVIEW

View Article Online
View Journal

Cite this: DOI: 10.1039/d6sc02126c

Layered oxide cathodes for sodium-ion batteries: origins of microcracks and countermeasures

Qiang Ma,[a] Ling-Yi Kong,*[b] Bang-Yuan Guo,[c] Qi-Lin Ran,[c] Ya-Fang Wang,[a] Yan-Fang Zhu[c] and Yao Xiao *[c]

Layered transition metal oxide cathodes (Na_xTMO_2) for sodium ion batteries have stood out among various cathode materials owing to their advantages in cost and electrochemical performance. However, their further practical application is hindered by deep-seated structural degradation, interfacial instability, and poor air stability. Among these issues, microcracks serving as a critical bridge between intrinsic defects in Na_xTMO_2 and macroscopic performance decay have emerged as a central focus of current research. Accordingly, this review systematically summarizes the origins of microcrack formation in Na_xTMO_2 and the corresponding mitigation strategies. The influence of primary structural defects introduced during material synthesis is first examined. Subsequently, the structural and chemical roots of microcrack formation during electrochemical processes are elucidated. Finally, crack formation pathways induced by environmental factors and interfacial evolution, particularly those associated with air exposure and cathode–electrolyte interfaces, are discussed. Building on these mechanistic insights, we critically compare current suppression strategies, including electronic structure regulation, lattice strain engineering, and interfacial engineering. The failure mechanisms and mitigation approaches related to microcracks summarized in this review are expected to contribute to the overall performance enhancement of Na_xTMO_2 and to provide important guidance for their industrial application in sodium-ion batteries.

Received 14th March 2026
Accepted 17th April 2026

DOI: 10.1039/d6sc02126c

rsc.li/chemical-science

1 Introduction

With the growing demand for large-scale energy storage and new types of power systems, sodium-ion batteries (SIBs) are gaining attention as an important complementary solution to lithium-ion batteries (LIBs) by virtue of the advantages of abundant resources, low cost, and relative safety of the system.[1] Among them, SIB cathode materials represented by layered transition metal oxides for sodium-ion batteries (Na_xTMO_2) are considered to be a class of cathode materials with the most promising prospects for industrialization due to the advantages of high reversible capacity, high operating voltage and a mature preparation process.[2,3] However, compared with the LIB system, Na^+ has a larger ionic radius, which makes Na_xTMO_2 more prone to dramatic lattice distortion, phase structure degradation, and anionic redox irreversibility during cycling, leading to more complex phase transition behavior and rapid performance decay.[4–6]

In terms of crystal structure, Na_xTMO_2 consists of transition metal (TM) layers stacked alternately with Na layers. According to the coordination environment in which Na^+ is located and the stacking mode of the oxygen layer, Na_xTMO_2 can be divided into O3, P2, P3 and other structural types of oxides.[7–9] During the charging and discharging process, the repeated de-embedding of Na^+ drives the relative slip of the TM layers and induces periodic changes in the layer spacing and TM–O bond length.[10–12] In particular, under high voltage and deep desodiation conditions, various phase transitions are often accompanied by strong anisotropic lattice strains, resulting in the formation of a complex multiphase coexistence and strain gradient field inside the particles, in addition to the irreversibility of the structural evolution that is further exacerbated by the concomitant Na^+/TM migration and oxygen anionic redox reactions. These structural features make the lattice framework of Na_xTMO_2 flexible but easy to be destabilized in the sense of chemical–mechanical coupling, and once the local stress cannot be released in time, stress relaxation often occurs in the form of dislocations, twins, phase boundary migration, and even macroscopic cracks.[13–16]

In recent years, a large number of *in situ* and *ex situ* characterization studies have shown that microcracks generated during cycling are one of the key factors in the failure of Na_xTMO_2.[17,18] Within the primary particles, the sites of stress

[a]College of Materials Engineering, Henan International Joint Laboratory of Rare Earth Composite Materials, Henan Key Laboratory of Electronic Ceramic Materials and Application, Henan University of Engineering, Zhengzhou, Henan 451191, P. R. China. E-mail: maqiang@haue.edu.cn

[b]College of Chemical Engineering, Sichuan University, Chengdu, 610065, P. R. China. E-mail: konglingyi@stu.scu.edu.cn

[c]College of Chemistry and Materials Engineering, Wenzhou University, Wenzhou, 325035, P. R. China. E-mail: xiaoyao@wzu.edu.cn

concentration due to uneven Na^+ (de)intercalation and defect enrichment are often the first to produce cracks, while in secondary particles, the stress accumulation between grains and at grain boundaries tends to induce particle rupture. The appearance of cracks not only changes the local stress distribution, but also amplifies the structural instability originally confined to the interior of the crystal to the entire electrode by exposing fresh interfaces and destroying the electrode film and conductive network. Specifically, cracks significantly increase the contact area between particles and electrolyte, induce violent interfacial side reactions, and lead to repeated rupture and reorganization of cathode electrolyte interphase (CEI)/solid electrolyte interphase (SEI) membranes, resulting in rising interfacial impedance and continuous loss of active Na.[19,20] At the same time, cracks and holes provide channels for oxygen escape, gas aggregation and localized thermal runaway, exacerbating the safety risk. With the advancement of cycling, the structural and interfacial degradation triggered by microcracks will gradually accumulate, which will ultimately be manifested in the simultaneous deterioration of energy density and lifetime of the whole battery. However, previous studies have mostly focused on material composition, phase-transition chemistry, oxygen redox, or interfacial degradation as separate topics, while microcracks are often treated only as one manifestation of failure rather than as the central thread linking these processes across multiple length scales.[21,22] In this Review, we place microcracks at the center of the discussion and use them as a cross-scale descriptor connecting synthesis-derived defects, electrochemically driven structural evolution, environmental/interfacial corrosion, and electrode-level performance decay. By organizing the literature from the perspective of crack origin, propagation, and suppression, this Review aims to provide a more integrated mechanistic framework for the rational design of high-energy-density and long-lifetime Na_xTMO_2 cathodes.[23–25]

2 Formation of microcracks

To explore the mechanism of performance degradation in sodium ion battery layered transition metal oxides (Na_xTMO_2), a large number of articles have been published on microcracking, which indicates that the antecedents and consequences of microcracking have received much attention from researchers (Fig. 1a). Based on this, we will also provide a systematic summary of what is relevant. Microcracks in Na_xTMO_2 usually originate as a result of an imbalance between the stress field and the local strength of the material induced by chemical and structural evolution.[26,27] As shown in Fig. 1b, from the available studies, the causes leading to microcracks can be traced back to three levels: first, primary defects such as microstrain, dislocations, and stacked laminations introduced during the material synthesis process; second, structural defects caused by corrosive effects in air and electrolyte environments in combination with mechanical stresses; third, phase transitions, interlayer slip, Na^+/TM migration with anionic redox behaviors induced due to intercalation, and migration of Na^+/TM during electrochemical processes. Therefore, clarification of the above three types of origins will help to increase the understanding of the structural degradation mechanism of layered oxide cathodes for sodium-ion batteries (SIBs).

2.1 Origin of microcracks during material synthesis

In contrast to the structural and chemical evolution during electrochemical processes, Na_xTMO_2 may carry significant

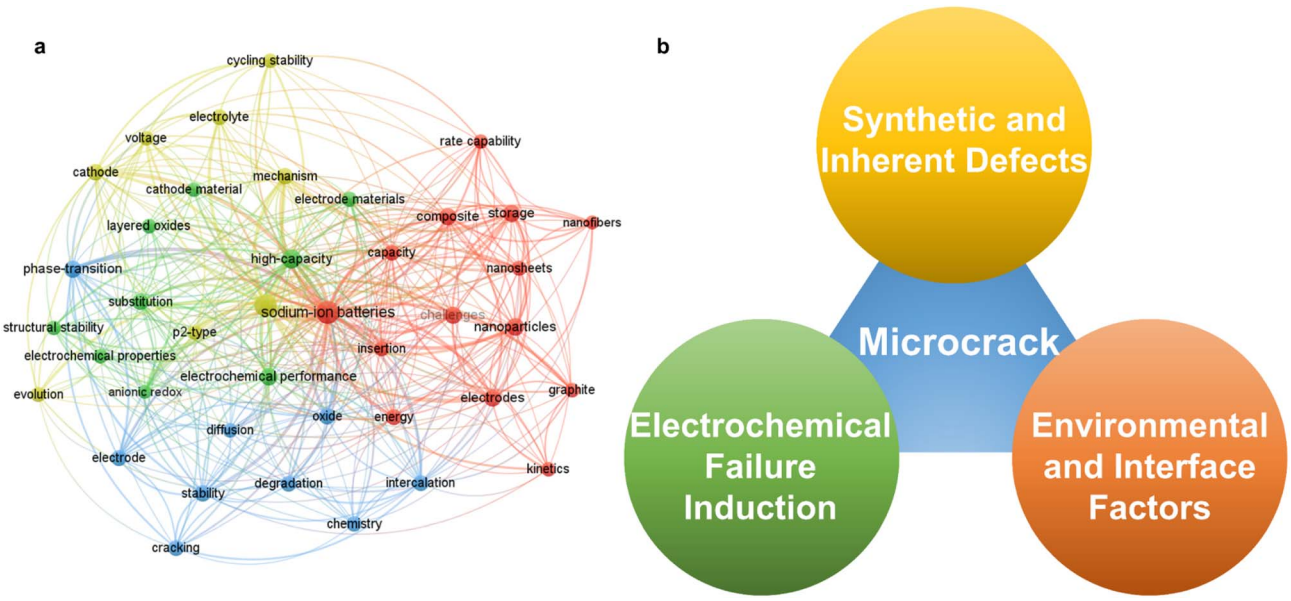

Fig. 1 (a) Research hotspots of crack in layered oxide cathodes from 2016 to April 2026 (the data were collected *via Web of Science*, January 2026). (b) Three contributing factors to microcrack initiation in sodium-based layered oxide cathodes: synthetic and inherent defects (residual microstrain, stacking faults from processing); electrochemical behavior induction (phase-transition/slab-glide driven anisotropic strain and stress accumulation); environment and interface factors (air/electrolyte corrosion and reconstructed shells enabling stress–corrosion feedback).

microstrain and crystal defects at the synthesis and initial processing stages. These primary structural features can significantly affect the threshold and pathway of microcrack formation under stress during subsequent electrochemical processes. Factors such as precursor composition homogeneity, primary/secondary particle morphology, phase transition and temperature gradient during sintering, cooling rate, and atmosphere control can leave residual stresses, dislocations, and stacked laminar faults in the product that are difficult to be completely eliminated by subsequent treatment.[28–31]

Using full-field 3D transmission X-ray microscopy (TXM) coupled with X-ray absorption near-edge structure (XANES) spectroscopy, Amine *et al.* proposed microstrain screening as an idea for evaluating the initial stress state inside the particles. Comparison of a series of Na_xTMO_2 with the same composition but different synthesis processes reveals that some particles have a clear concentration of high microstrain regions inside the particles, which spatially tend to correspond to a slight segregation of precursor compositions, incomplete elimination of multiphase reactions, or localized sintering insufficiency.[32] In contrast, some other particles exhibit a more uniform strain distribution and a lower overall level. During subsequent electrochemical cycling, the former particles are more prone to preferential dislocation slip, localized phase transitions, and crack initiation in the high-strain regions, while the latter particles show structural failure only at a higher number of cycles. These results suggest that the primary microstrain itself constitutes a reserved stress field, which when superimposed with the subsequent electrochemically induced strain can significantly lower the threshold for crack formation. The first-cycle charge–discharge process is often a critical stage for the activation and rearrangement of primary microstrain and defect structures (Fig. 2a and b). Amine *et al.* also found that the average lattice parameter of some Na_xTMO_2 materials (O3–$NaNi_{0.4}Mn_{0.4}Co_{0.2}O_2$) did not change drastically in the first cycling process, but a large number of new dislocations, stacking faults, and layer defects were generated inside the grains, and the strain field undergoes significant remodeling.[33] These nascent defects become preferential crack-generating sites in subsequent cycles, causing the material to exhibit only a slow capacity decay in early cycling, but a sudden change in behavior similar to structural collapse after a certain number of cycles (Fig. 2c and d). From this perspective, both stages of synthesis and first cycles have a significant impact on the defect and strain distribution within the particle, laying the structural foundation for the formation of subsequent crack networks.[34]

2.2 Origin of microcracks upon cycling

In Na_xTMO_2, deep desodiation is usually accompanied by significant structural and chemical evolution.[35–38] These evolutions manifest macroscopically as a series of phase transitions and interlayer slip such as P2–O2, P2–OP4, O3–P3, *etc.* At the microscopic level, they involve various pathways such as the ordered–disordered transformation of Na^+/vacancy, Na^+/TM migration, and anionic redox behavior.[39–42] These evolution processes can be reversible within a reasonable voltage window and structural constraints, but under extreme conditions, they often occur in a highly non-uniform and strongly coupled manner, thereby affecting the unit cell parameters, local coordination environment, and bond strength. Thus, this chemical process will establish an anisotropic elastic strain field and a highly concentrated chemical stress field within the particles.[43] When the strength of the superposition of these two fields exceeds the local fracture critical point, microcracks will emerge in the interface region.[44–46]

From the perspective of structural evolution, phase transition and interlayer slip are among the most direct sources of electrochemically driven stresses.[47,48] *In situ* X-ray diffraction (*in situ* XRD) and structural analysis based on Na_xTMO_2 show that the *a*-axis changes during charging are relatively mild, while the *c*-axis shrinkage often reaches several percentage points or even higher, reflecting much larger volume changes along the interlayer direction than in the in-plane direction.[49] For individual grains, such a volumetric anisotropy change implies that even if the overall phase transition is reversible, the strains between different regions within the grain are difficult to be coordinated by uniform elastic deformation. As a result, once the phase transformation becomes asynchronous in time and space, the phase boundaries and their neighboring regions are prone to accumulate large internal stresses, which can induce microcracks. Regarding this, Somerville *et al.* used $Na_{2/3}[Ni_{1/3}Mn_{2/3}]O_2$ and P2–$Na_{2/3}[Ni_{1/6}Mn_{1/2}Fe_{1/3}]O_2$ as models, using *in*

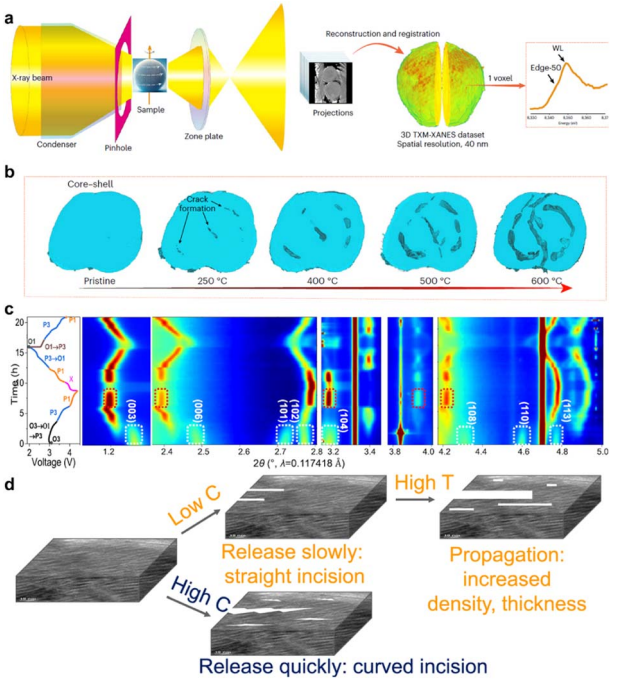

Fig. 2 (a) Schematic illustration of full-field 3D TXM-XANES measurement and data reconstruction; (b) *in situ* 3D TXM-XANES results of $Ni_{0.8}Mn_{0.1}Co_{0.1}(OH)_2$ during calcination. Reprinted with permission from ref. 32 Copyright 2024, Springer Nature. (c) Contour plot of *in situ* SXRD patterns for O3–$NaNi_{0.4}Mn_{0.4}Co_{0.2}O_2$ across the 2–4.4 V voltage range; (d) schematic diagram of the nanogap morphology of O3–$NaNi_{0.4}Mn_{0.4}Co_{0.2}O_2$ during cycling. Reprinted with permission from ref. 33 Copyright 2022, Springer Nature.

situ XRD and FAULTS fitting to reveal that the former underwent a P2–O2 phase transition above approximately 4.1 V, with TM–O interlayer slip accompanied by a significant rightward shift and significant broadening of the (002) peak, indicating a strong anisotropic volume mutation.[50] While the latter introduced the OP4/Z phase as an intermediate layered stacking, the Na desorption process showed an asymptotic evolution of P2–OP4–O2, with a smaller and more continuous overall *c*-axis contraction. At the same Na deintercalation depth, the different phase transition paths thus correspond to very different strain magnitude and spatial gradient distributions, providing different structural initial conditions for the subsequent susceptibility to the formation of strain concentrations and microcracks (Fig. 3a–c). In P2–$Na_{2/3}Ni_{1/3}Mn_{2/3}O_2$, Sui *et al.* observed a more direct correlation between phase transition and crack formation.[51] Through electron diffraction and crystal plane spacing analysis, the (002) crystal plane spacings of P2 and O2 phases were measured to be approximately 5.6 Å and 4.4 Å, respectively, with the contraction along the interlayer direction being much larger than the change in the lattice parameters in the plane direction. In the coexistence of P2/O2, scanning transmission electron microscopy (STEM) showed significant lattice mismatch and strain concentration near the phase boundary and related to the layered stacking, with the cracks preferentially located at these phase boundaries and related to the specific crystal directions, and gradually extending into the grain interior in subsequent cycles, eventually evolving into a crack network throughout the particle (Fig. 3d–f). This work clearly shows that the anisotropic strain induced by the P2–O2 phase transition is difficult to be fully released at the phase boundaries by localized elastic relaxation, and that microcracks sprouting and expanding become an important pathway to release the internal stresses driven by the phase transition (Fig. 3g). In O3-type materials, phase transformation is also one of the core reasons for the generation of microcracks. Yu *et al.* took O3–$Na[Ni_{0.5}Mn_{0.5}]O_2$ as an example and demonstrated through *in situ* XRD and morphology characterization that this material undergoes multiple phase transitions such as O3–O′3–P3–P′3 during the charging process.[52] Among them, the phase transformation from P3′ into O3′ accompanied by a significant *c*-axis change and peak shape broadening is the key stage of rapid capacity decay. Meanwhile, under the conditions of high cutoff voltage and multi-turn cycling, a large number of cracks extending along the grain boundaries and intracrystalline can be observed inside the secondary particles of the material, and the secondary particles are gradually cut and pulverized (Fig. 3h). Therefore, it can be found that the phase transition front tends to first appear at grain boundaries while the pristine phase is still retained in the interior, resulting in a significant strain gradient in the radial direction. While the phase transition front advances within the grains, this strain gradient continues to accumulate along a particular grain surface or grain boundary, which ultimately evolves into macroscopically visible microcracks in the cycle.[57] In

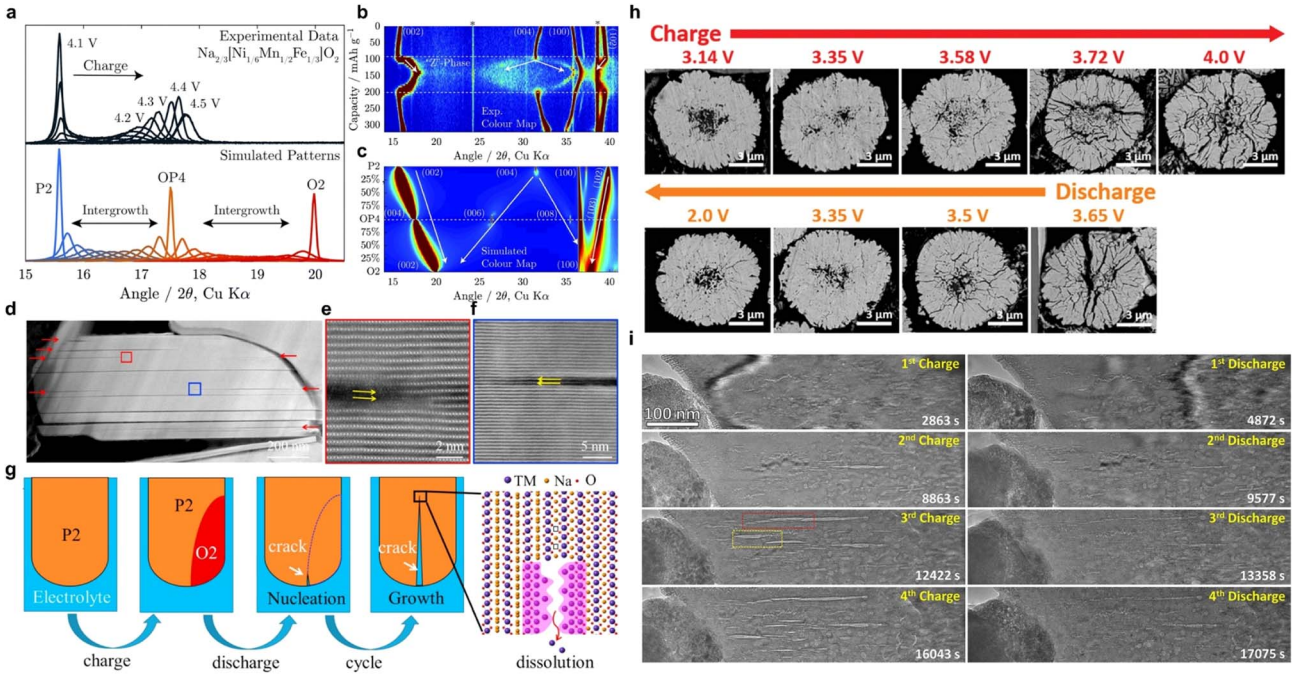

Fig. 3 (a and b) *In situ* XRD results for $Na_{2/3}[Ni_{1/6}Mn_{1/2}Fe_{1/3}]O_2$ and corresponding fault simulation results; (c) intensity contour map (bird's eye view) of $Na_{2/3}[Ni_{1/6}Mn_{1/2}Fe_{1/3}]O_2$ and its color-mapped representation over a wider 2*y* range. Reprinted with permission from ref. 50 Copyright 2019, Royal Society of Chemistry. (d) HAADF-STEM observation of in-grain cracks formed in P2–$Na_{2/3}Ni_{1/3}Mn_{2/3}O_2$ after cycling and (e and f) corresponding atomic resolution images; (g) schematic diagram showing crack's nucleation and growth. Reprinted with permission from ref. 51 Copyright 2018, Elsevier. (h) SEM images of $Na[Ni_{0.5}Mn_{0.5}]O_2$ at different charge/discharge states during the first cycle. Reprinted with permission from ref. 52 Copyright 2020, John Wiley and Sons. (i) *In situ* TEM images of the structural evolution of $Na_{0.7}Ni_{0.3}Mn_{0.6}Co_{0.1}O_2$ during four charge–discharge cycles. Reprinted with permission from ref. 53 Copyright 2021 American Chemical Society.

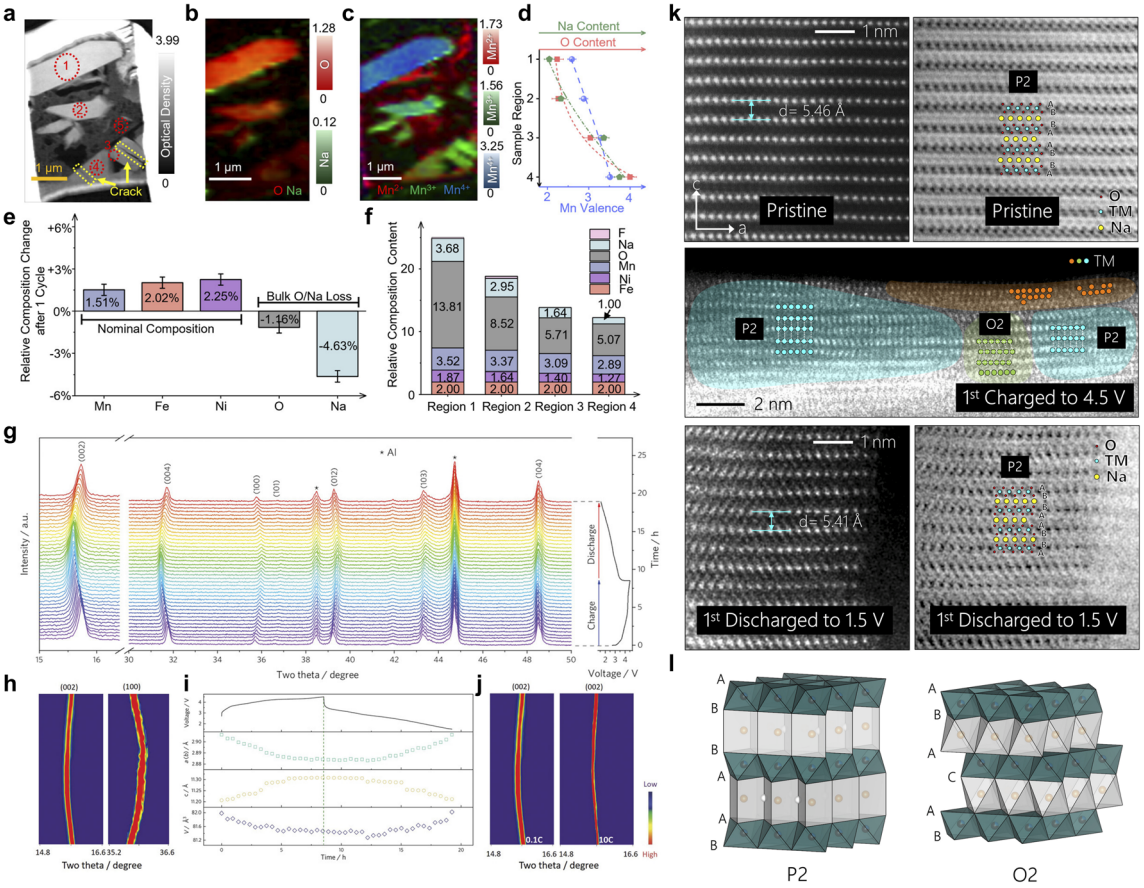

Fig. 4 (a) Averaged ptychography amplitude image from all elemental edges; color composite map of conventional STXM images from the (b) O and Na K-edge, (c) Mn^{2+}, Mn^{3+}, and Mn^{4+} edges; (d) trends in Mn oxidation states and distribution of O and Na content across different sample regions; (e) compositional changes in Mn, Fe, Ni, O, and Na after cycling; (f) quantitative XAS analysis in different regions. Reprinted with permission from ref. 54 Copyright 2025, American Chemical Society. (g) *In situ* XRD patterns of P2–$Na_{0.7}Mg_{0.2}[Fe_{0.2}Mn_{0.6}\square_{0.2}]O_2$ in the voltage range of 1.5–4.5 V (0.1C), along with (h) the corresponding contour plots and (i) evolution of lattice parameters; (j) contour plots of the evolution of the (002) peak at 0.1 and 10C. Reprinted with permission from ref. 55 Copyright 2021, John Wiley and Sons. (k) HAADF STEM images of $Na_{0.72}[Li_{0.24}Mn_{0.76}]O_2$ of different charge/discharge states on the particle surface; (l) schematic diagram of P2 and O2 structures. Reprinted with permission from ref. 56 Copyright 2019, Elsevier.

$Na_{0.7}Ni_{0.3}Mn_{0.6}Co_{0.1}O_2$, Huang *et al.* observed by *in situ* transmission electron microscopy (*in situ* TEM) that the TM–O layer appeared to be significantly arched and folded in localized regions to form a kinking structure, with significant changes in layer spacing along the kink bands with interlayer bonding. Under the repeated accumulation of stresses during cycling, the local strains near these kink bands are often difficult to be completely eliminated by elastic recovery, thus gradually evolving crack initiation.[53] This result shows that internal localized layer slip and deformation may also be the initiation location of microcracks even in the absence of an obvious phase transition front.[58]

In addition to the above structural drivers, the chemical stresses introduced by Na^+/TM migration and anionic redox further exacerbate the inhomogeneity of the stress field. Liu *et al.* show that for O3–$NaLi_{1/9}Ni_{2/9}Fe_{2/9}Mn_{4/9}O_2$ the charge compensation mechanisms in different regions within the particles are significantly different during the high voltage charging process.[54] Certain regions are dominated by O-redox, accompanied by the formation of O–O short bonds, local oxygen vacancy generation and volume contraction, while some other regions mainly rely on the oxidation of TM with relatively mild structural distortion. Scanning transmission X-ray microscopy (STXM) imaging further reveals that after multiple cycles, the former regions tend to exhibit increased stiffness and structural densification, while the latter remain relatively soft, with hard–soft interfaces forming between the two, where stress concentrations are significantly higher than the material average, and cracks are often preferred along the paths with the largest gradients in chemistry and valence states (Fig. 4a–f). The aforementioned studies have shown that when the O-redox is strongly coupled to Na^+/TM migration and shows a high degree of spatial localization, it is often accompanied by significant local volume contraction and stiffness changes, which are important sources of chemical stresses during electrochemical processes. However, it has also been shown that the anionic redox behavior can be transformed into a low-strain form by the design of the electronic structure and local coordination, thus

significantly attenuating its driving force for microcracking. Taking P2–$Na_{0.7}Mg_{0.2}[Fe_{0.2}Mn_{0.6}\square_{0.2}]O_2$ as an example, Li *et al.* constructed local coordination units such as Na–O–□, Mg–O–□, and so on, by introducing Mg as a strut and TM vacancies in the Na layer, so that the charge compensation proceeds reversibly in a near-solid solution manner within a wide voltage window of 1.5–4.5 V. The P2 phase is always maintained throughout the cycling process, which exhibits only minimal lattice parameter changes and mild structural transitions, and no drastic laminar phase transitions, such as P2–O2, are observed (Fig. 4g–j).[55] Similarly, P2–$Na_{0.72}[Li_{0.24}Mn_{0.76}]O_2$ stabilizes high-valent Mn with O-redox with the help of Li–O–Li localized configuration, and its structural evolution is still confined to a limited magnitude of lattice strain while obtaining a high capacity of more than 200 mAh g^{-1}.[56] Meanwhile, none of the morphological characterization techniques such as STEM showed severe particle pulverization and crack networks (Fig. 4k and l). This type of low-strain O-redox system suggests, conversely, that it is not the participation of oxygen anions in the charge compensation process *per se* that really drives microcracking, but whether it is accompanied by a drastic and spatially highly non-uniform bulk response.[59] Homogenization of anionic redox reactions and weakening of the chemical stress gradient through compositional and local coordination engineering are expected to significantly reduce the microcracking tendency during electrochemical processes while maintaining high energy densities.[60]

2.3 Environmentally and interface-induced cracks

Under actual electrode processing and battery operating conditions, Na_xTMO_2 is not only subjected to internal stresses from electrochemical processes, but also to exposure to complex chemical environments such as humid air, CO_2, and electrolytes and their decomposition products.[61–63] Under the combined effect of mechanical stress and chemical attack, Na_xTMO_2 may undergo stress corrosion cracking similar to that found in conventional alloys and ceramics, *i.e.*, in the presence of corrosive media, the mechanical threshold required for crack initiation and expansion is significantly reduced. For Na_xTMO_2, air exposure, electrolyte decomposition, and thermally induced decomposition at high states of charge (SOC) are currently among the core causes driving microcracking at the environmental and interfacial levels.[66,67]

Among many environmental factors, air sensitivity is one of the most typical and difficult to circumvent problems of Na_xTMO_2. It has been shown that after Na_xTMO_2 is exposed to humid air, Na^+/H^+ exchange occurs rapidly, generating residual bases such as sodium carbonate and sodium hydroxide on the surface of the material, accompanied by some cation mixing and local structural remodeling, which results in the formation of corrosive phases on the surface layer of the particles with a composition and structure significantly different from that of the main laminar phase.[68] The differences in lattice parameters and elastic modulus between these corrosive phases and the internal lamellar phase result in significant residual stresses at the interface between the two, and these interfacial regions are prone to become crack initiation sites during the subsequent charge/discharge process under the combined effect of volume changes and the external environment. Against this backdrop, fine nanoscale studies reveal how the corrosive phases caused by humid air can be used as the microcrack initiation regions. Manthiram *et al.* used O3–$NaNi_{0.7}Mn_{0.15}Co_{0.15}O_2$ as a research model and showed that in humid air Na^+ continues to migrate out of the bulk structure, and the particle surface sequentially accumulates NaOH, Na_2CO_3, and its hydrate, accompanied by the dissolution of Ni to produce NiO.[64] This corresponds to the coating of a multilayer insulating layer of residual alkali and NiO outside the laminate bulk corrosion shell layer (Fig. 5a and b). Further interface chemical analysis shows that the residual alkali group will undergo a de-fluorination reaction with the PVDF binder, generating NaF and significantly weakening the overall adhesion strength of the electrode. This can easily translate into extended stress corrosion cracks along the shell–body interface under volume changes and external forces from subsequent electrochemical cycling. More recently, a systematic study of O3–$NaNi_{1/3}Fe_{1/3}Mn_{1/3}O_2$ by Hu *et al.* took a more macroscopic view to distinguish the roles of different air components in the corrosion process and directly observed the

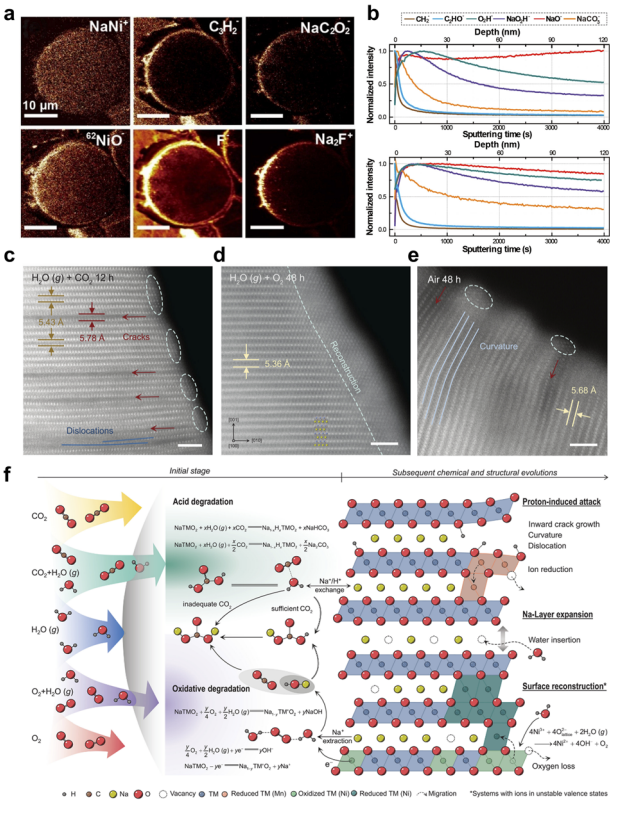

Fig. 5 (a and b) TOF-SIMS spectrum of the O3–$NaNi_{0.7}Mn_{0.15}Co_{0.15}O_2$ electrode after 24 hours of exposure. Reprinted with permission from ref. 64. Copyright 2018, American Chemical Society. STEM images of $NaNi_{1/3}Fe_{1/3}Mn_{1/3}O_2$ after storage for 12 hours in (c) water vapor, and for 48 hours in (d) O_2 and water vapor and (e) humid air; (f) schematic diagram of the degradation mechanism of Na_xTMO_2 in air. Reprinted with permission from ref. 65. Copyright 2024, American Association for the Advancement of Science.

coupling between chemistry and microcracking evolution in humid air.[65] The results show that water vapor alone triggers more reversible hydration and surface adsorption, while the $H_2O + CO_2$ combination drives acidic corrosion with Na^+/H^+ exchange, forming regions of proton enrichment and Mn valence reduction. $H_2O + O_2$ triggers oxidation–reduction cycles and surface rock salt-like remodeling. STEM reveals that these proton-enriched and remodeled zones tend to spatially correspond to the hotspots of interlayer bending and localized expansion, which become preferred locations for crack germination and expansion in subsequent electrochemical cycles (Fig. 5c–e). More importantly, this work proposes composition–structure design guidelines targeting the reduction of cation competition coefficients, optimization of the operating voltage window, and particle scaling, which provide quantitative references for the reduction of environmentally driven microcracks from the external dimension of air chemistry (Fig. 5f).

At the electrode–electrolyte interface, chemical reactions and mechanical stresses combine to cause the generation of microcracks.[69,70] Polarization decomposition of the carbonate electrolyte at high voltage generates acidic species such as HF and strong oxidizing intermediates, and these reactive components preferentially attack the high-energy crystal surfaces and grain boundaries exposed to the electrolyte, triggering a continuous loss of Na^+ and dissolution of TM and driving the gradual reconfiguration of the surface layer from layered to rock–salt or anti-spinel phases. As a result, a heterogeneous interfacial layer with low Na content, high TM valence and defect density, and significantly worse ionic conductivity and ductility than the main layered phase is formed, which causes the main layered-phase interface to experience higher stress concentration in the subsequent volume change, thus generating the risk of microcrack initiation. On this basis, a positive feedback loop readily forms between the phase transformation of the bulk phase and the interfacial corrosion. The internal stresses accumulated by the phase transition and anisotropic bulk response during cycling preferentially drive microcrack generation near the defects and grain boundaries of the interfacial layer. At the same time, once the microcracks are generated, the cracks will provide a high-flux channel for the intrusion of the electrolyte, and the freshly exposed internal surfaces will undergo accelerated corrosion and secondary remodeling, generating a new, mechanically more fragile rock-salt/anti-spinel interfacial layer. As the cycle advances, the interfacial layer thickens and becomes brittle, and the crack tip expands to the deeper part of the particle under the dual driving force of stress concentration and localized chemical erosion, manifesting an evolutionary path in which crack expansion and interfacial degradation are mutually reinforcing, thus transforming the microcrack from a mere by-product of bulk phase transition into a key source of environmentally induced structural failure. Interfacial engineering and electrolyte design confirm this understanding from the opposite side. Wei *et al.* constructed a composite electrolyte of gel polymer electrolytes and 4-trifluoromethylphenylboronic acid, so that PF_6^- preferentially decomposed at the interface to form NaF and B-containing inorganic complexes, and then the organic–inorganic composite CEIs were obtained, which were mainly inorganic, with a moderate thickness and spatial distribution uniformity.[71] Compared with the thick, soft and complex CEI formed under the traditional liquid electrolyte, the interfacial film remains continuous and dense under high voltage and long cycling conditions, which significantly suppresses interfacial corrosive cracking and particle edge cracking (Fig. 6a). Similarly, the inorganic enriched SEI/CEI constructed using weakly polar solvents coupled with high concentrations of NaFSI effectively weakened HF generation and TM dissolution, so that the interfacial layer no longer experienced drastic side reactions (Fig. 6b and c).[72] From the perspective of microcrack origin, when the interface chemistry is confined in a protective layer with a continuous structure and high modulus, the positive feedback chain of crack generation–electrolyte infiltration–localized corrosion–interfacial embrittlement–crack extension will be significantly weakened, and the threshold of environment- and interface-induced microcrack generation will be significantly elevated as a result.[73] In addition, under high SOC and external abuse conditions, thermally induced oxygen release and structural remodeling constitute an extreme case of environment–mechanics coupling. *In situ* high-temperature TEM analysis of P2–$Na_{0.8}Ni_{0.33}Mn_{0.67}O_2$ shows that with increasing temperature, lattice oxygen is gradually released, and the structure is transformed from a layered into a rock-salt or more disordered phase, which is accompanied by localized pore generation and drastic volume contraction (Fig. 6d and e).[74]

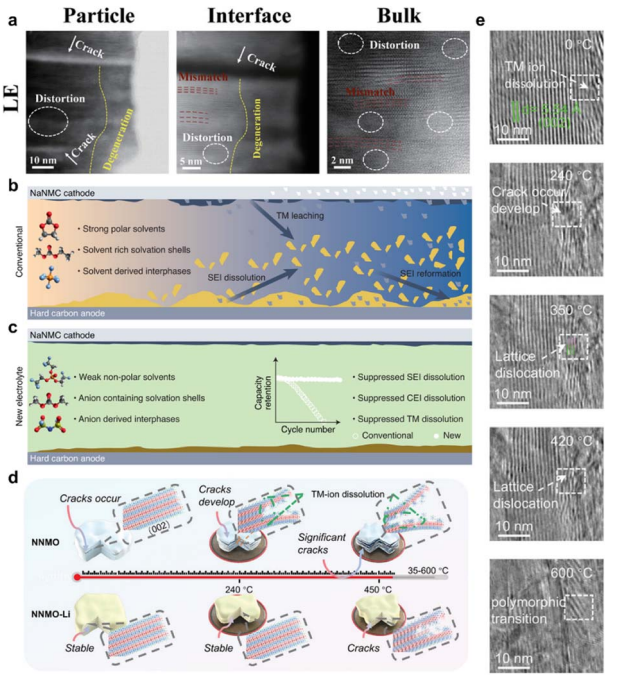

Fig. 6 (a) Failure analysis of Na_xTMO_2 cathodes in different electrolytes. Reprinted with permission from ref. 71 Copyright 2023, John Wiley and Sons. (b and c) Effects of different electrolytes on the SEI. Reprinted with permission from ref. 72 Copyright 2022, Springer Nature. (d) Schematic diagram illustrating the thermal decomposition of the desodiated Na_xTMO_2; (e) *in situ* high-temperature TEM of P2–$Na_{0.8}Ni_{0.33}Mn_{0.67}O_2$. Reprinted with permission from ref. 74 Copyright 2025, John Wiley and Sons.

This process is prone to generate a large number of new cracks or promote the rapid expansion of existing cracks, posing a significant threat to the thermal safety of the cell.

Overall, environmental and interfacial reactions lower the mechanical threshold for microcrack initiation in Na_xTMO_2 by altering local composition, structure, and mechanical properties, thereby accelerating crack nucleation and propagation through stress–corrosion coupling. From a practical perspective, several environmental variables should be prioritized for control. First, humid-air exposure time and humidity level should be minimized during powder handling, electrode processing, and storage, because prolonged exposure promotes Na^+/H^+ exchange and the buildup of residual alkali species. Second, the roles of H_2O and CO_2 should be distinguished, as H_2O mainly induces hydration and adsorption, whereas H_2O + CO_2 more readily drives acidic corrosion and proton-enriched surface degradation. Third, the residual alkali level should be carefully monitored, because it can trigger parasitic reactions with binders and electrolytes and further weaken interfacial mechanical integrity. Fourth, electrolyte chemistry, especially HF generation tendency and CEI composition, should be optimized to suppress corrosion-assisted crack growth. Finally, special attention should be paid to highly desodiated or high-SOC states, where thermal instability, oxygen release, and rapid surface reconstruction can sharply increase crack sensitivity. These factors provide a more actionable framework for reducing environmentally and interfacially induced microcracks in practical Na_xTMO_2 systems.[75–77]

3 Microcrack suppression and material design strategies

With strategies for microcrack inhibition and material design after exploring the multiple sources of microcracks, further research is needed on how to weaken the chemical and structural stresses that drive the formation of microcracks through material and electrode design, and to enhance the material's tolerance to microcracks. The existing research can be summarized from three dimensions: first, the regulation of the electronic structure, by controlling the properties of TM–O bonds, the arrangement of Na^+/vacancies, and the O-redox behavior, to weaken the harmful phase transitions and volume changes at the chemical level; second, the engineering of lattice strain and phase pathway, by designing near-zero-strain reaction pathways, constructing heterostructures, and optimizing stacking patterns, to alleviate anisotropic deformation at the crystallographic level; finally, the engineering of the interface, to disperse stress, block crack propagation channels, and stabilize the interface environment at the particle and electrode scales.[78–81]

3.1 Electronic structure guided crack suppression

In Na_xTMO_2 cathodes, the Na content, TM valence combination, and oxygen anions together determine the phase transition path, lattice strain, and structural stability. Numerous studies have shown that if the driving force of irreversible phase transition and irreversible anionic redox is reduced at the electronic structure levels, and the strain distribution is homogenized at the local scale, the microcrack generation and extension inside and on the surface of the particles can be significantly suppressed.[82,83]

From the phase diagram point of view, the Na content and the total amount of TM together determine the average TM valence state as well as the possible phase transition paths. Modulation of the Na/TM ratio and TM valence state is one of the effective means to suppress microcracking. High Na content can enhance the shielding of Na^+ against the interlayer coulombic repulsion of TMO_2, and reduce the tendency of interlayer slip and *c*-axis collapse during deep desodiation. Meanwhile, reasonable control of the average valence state of TM can mitigate irreversible oxidation and oxygen release in the high-voltage region. To address this point, Hu *et al.* found that P2–$Na_{45/54}Li_{4/54}Ni_{16/54}Mn_{34/54}O_2$ with high Na content maintains a single P2 phase and highly reversible lattice parameter evolution after long cycling.[84] Moreover, neither the P2–O2 nor the P2–OP4 phase transition is observed, which reduces the driving force for stress accumulation and crack extension at the structural level, and provides better structural integrity than conventional Na-containing P2 materials' (Fig. 7a). In a similar line of thought, Qiao *et al.* synthesized $Na_{0.7}Fe_{0.1}Mn_{0.75}\square_{0.15}O_2$ by introducing an appropriate amount of TM vacancies into the $Na_{0.7}Fe_{0.33}Mn_{0.67}O_2$ system, so that a part of the local charge compensation is borne by the Na^+/vacancy rearrangement instead of stress relief through long-range layered stacking transitions, which can maintain the P2 structure within a wide voltage window and avoid the significant P–O phase transition.[85] Quantitatively, the vacancy-doped sample delivers 70.1% capacity retention after 200 cycles at 1C (2.0–4.3 V), and *in situ* XRD shows a much smaller (002) peak shift than the vacancy-free counterpart, indicating substantially suppressed *c*-axis strain swing during charge. And the degree of pulverization and crack density of the particles after cycling are significantly lower than those of the vacancy-free samples (Fig. 7b–d). These results suggest that a reasonable combination of Na/TM ratio and TM vacancies can shift the charge compensation mode from a phase transition accompanied by drastic stack slip with large volume changes to a path dominated by local Na^+/vacancy rearrangement with limited lattice-scale strain, thus weakening the stress driving force of microcracks on a macroscopic scale.

Based on the appropriate Na/TM ratio, further modulation of the local structure and strain field by high-entropy design is another important route to suppress microcracks.[90,91] Doping can not only change the lattice parameters and charge compensation modes, but also influence the crack initiation and extension paths by constructing regions with specific mechanical properties and chemical stability inside and on the surface of particles through site-selective and polarization behaviors.[92,93] The site-selective doping study by Wei *et al.* showed that, in P2–$Na_{2/3}Ni_{1/3}Mn_{2/3}O_2$, introducing a small amount of Sr^{2+} into the Na layer or introducing Sr^{2+} together with high-valent Y^{3+}/Mo^{6+} into the TM layer can effectively suppress the irreversible P2–O2 phase transition at high voltage, significantly reduce lattice-volume change, and thereby mitigate internal stress accumulation and microcrack

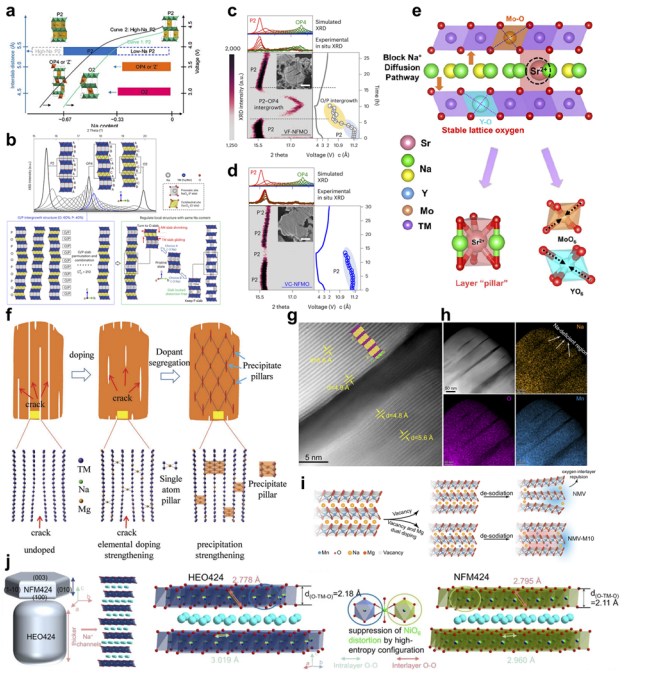

Fig. 7 (a) Structural evolution mechanism of high-sodium P2 oxides in electrochemical processes. Reprinted with permission from ref. 84 Copyright 2020, American Chemical Society. (b) Schematic diagram of the P–O phase transition; (c) *in situ* XRD patterns of $Na_{0.7}Fe_{0.33}Mn_{0.67}O_2$ and (d) $Na_{0.7}Fe_{0.1}Mn_{0.75}\square_{0.15}O_2$, along with corresponding FAULTS simulation results. Reprinted with permission from ref. 85 Copyright 2024, Springer Nature. (e) Schematic illustration of enhanced reaction kinetics induced by selective doping. Reprinted with permission from ref. 86 Copyright 2025, American Chemical Society. (f) Schematic illustration of the suppression effect of doping–segregation on interfacial microcracks. Reprinted with permission from ref. 87 Copyright 2019, John Wiley and Sons. (g) HAADF-STEM images and (h) corresponding EDS maps of $Na_8Mn_{11}O_{24}$ in the charged state; (i) schematic illustration of the structural evolution of $Na_{0.67}Mn_{0.011}[Mg_{0.1}\square_{0.07}Mn_{0.83}]O_2$ and $Na_8Mn_{11}O_{24}$. Reprinted with permission from ref. 88 Copyright 2025, Springer Nature. (j) Schematic diagrams of the morphologies of $NaNi_{0.25}Mg_{0.05}Cu_{0.1}Fe_{0.2}Mn_{0.2}Ti_{0.1}Sn_{0.1}O_2$ and $NaNi_{0.4}Fe_{0.2}Mn_{0.4}O_2$.[89] Copyright 2022, American Chemical Society.

formation (Fig. 7e).[86] Mechanistically, the total DOS indicates enhanced electronic conductivity by changing the electron distribution around the Fermi level, and the ELF analysis suggests that stabilized O–Sr coordination and electron localization effects around oxygen associated with Mo^{6+} promote oxygen-redox charge transfer. Accordingly, the cathode shows 85.8% retention after 2500 cycles at 20C and 99.2% retention after 800 cycles at 1C, even at −20 °C, while suppressing intergranular cracking. The spatial distribution of dopant elements also affects the microcrack evolution. The traditional view tends to pursue the complete homogeneity of doping, but in some systems, a moderate doping bias can play the role of mechanical reinforcement instead. The Mg-rich precipitated phase is formed in the Na layer during the cycling process, which constructs a three-dimensional "pillar"-like skeleton and changes the high-voltage structural evolution from the P2–O2 phase to the P2–OP4 phase with smaller volume change, thus significantly reducing the lattice strain associated with the phase transition and suppressing the generation of cracks inside the particles, which reflects the inhibition of the interfacial microcracks by doping–partitioning (Fig. 7f).[87] Another representative type of work is the synergistic regulation of anionic redox and structural evolution by TM vacancies and site engineering. In the P2–$Na_{0.67}MnO_2$ system, Amine *et al.* constructed Na–O–Mg and Na–O–□ conformations in the TM layer by introducing both Mg^{2+} and vacancies in the TM layer and inducing about 1.1% Mn ions to occupy the Na layer sites. This configuration can increase the number of non-bonded O 2p orbitals that are favorable for highly reversible anionic redox, inhibit the voltage decay caused by the Na–O–□ configuration, and allow the Mn ions occupying the Na layer to act as "rivets" to the oxygen layer in the deeply desodiated state to limit the interlayer slip, thus enhancing the stability of the high-voltage structure and mitigating crack generation (Fig. 7g–i).[88] In this "near-zero-strain" design, the maximum lattice-volume variation is ∼1.47%, delivering 155.1 mAh g^{-1} (14 mA g^{-1}) and 87.5% retention over 200 cycles (140 mA g^{-1}). On the basis of the doping strategy, high-entropy layered oxides generalize the multidoping to an equimolar polycation configuration. In the case of high-entropy O3-type cathodes such as $NaNi_{0.25}Mg_{0.05}Cu_{0.1}Fe_{0.2}Mn_{0.2}Ti_{0.1}Sn_{0.1}O_2$, for example, the conformational entropy is significantly increased by introducing multiple transition metals in the TM layer and expanding the thickness of the TMO_2 layer as well as weakening the Jahn–Teller distortion and Na^+/vacancy ordering trends. *In situ* structural characterization reveals a more gentle phase transition and less lattice strain over a wider voltage window, with significantly fewer cracks inside the particles than in the comparison samples after long cycling (Fig. 7j).[89] These high-entropy configurations show more homogeneous structural evolution and crack distribution on the macroscopic level, which improves the crack initiation threshold and the overall crack resistance.[98,99] These doped and high-entropy systems exhibit compressed lattice strain, shorter residence time in the O–P biphasic region, and more homogeneous in-plane strain distribution. Taken together, recent high-entropy and multication designs further support the view that microcrack suppression is not merely a consequence of stronger average bonding, but also of a more spatially homogeneous chemo-mechanical response, a shortened residence time in highly strained biphasic regions, and a reduced tendency toward local structural deconstruction during cycling. These advances reinforce high-entropy design as a promising route for simultaneously stabilizing bulk phase evolution and lowering crack susceptibility in high-voltage sodium layered oxides.

The same compositional modification can correspond to different electronic structure responses.[100] If the charge compensation is mainly concentrated in a certain valence-sensitive TM or a certain narrow voltage interval, it is easy to cause local structural distortion and strain concentration. In contrast, if the charge compensation is dispersed to a wider energy level and spatial range by modulating the TM–O covalency and the involvement of anionic redox, a low-strain window can be constructed under the premise of high capacity. In this context, Zhao *et al.* demonstrated a typical behavior of this kind

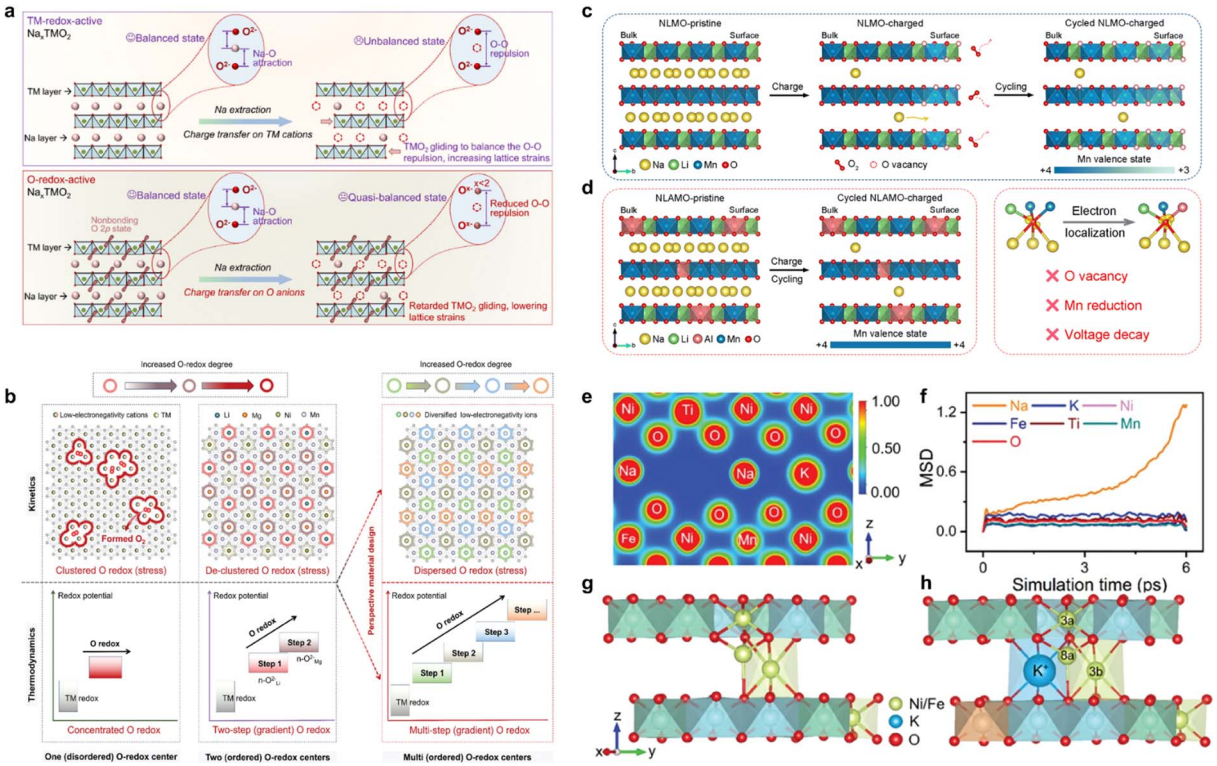

Fig. 8 (a) Schematic diagram of interlayer O–O repulsion changes during Na^+ deintercalation. Reprinted with permission from ref. 94 Copyright 2024, John Wiley and Sons. (b) Schematic comparison of oxygen reduction reactions between disordered $Na_{7/9}[Li_{1/9}Ni_{1/9}Mg_{1/9}Mn_{6/9}]O_2$ and ordered $Na_{7/9}[Li_{1/9}Ni_{1/9}Mg_{1/9}Mn_{6/9}]O_2$ structures, along with a schematic diagram illustrating the perspective design of materials featuring dispersed and multistage O redox. Reprinted with permission from ref. 95 Copyright 2024, John Wiley and Sons. Schematic illustration of anionic redox behavior and Mn oxidation state evolution in (c) $Na_{0.8}Li_{0.24}Mn_{0.76}O_2$ and (d) $Na_{0.8}Li_{0.24}Al_{0.03}Mn_{0.73}O_2$, along with the voltage decay suppression effect of Al in oxygen electron localization. Reprinted with permission from ref. 96 Copyright 2024, Royal Society of Chemistry. (e) Charge density contour map on the (102) crystal plane in O3–$Na_{0.898}K_{0.058}Ni_{0.396}Fe_{0.098}Mn_{0.396}Ti_{0.092}O_2$; (f) time evolution curves of the displacement of each element in O3–$Na_{0.898}K_{0.058}Ni_{0.396}Fe_{0.098}Mn_{0.396}Ti_{0.092}O_2$; (g) TM migration path in $Na_{0.987}Ni_{0.396}Fe_{0.204}Mn_{0.402}O_2$ and (h) O3–$Na_{0.898}K_{0.058}Ni_{0.396}Fe_{0.098}Mn_{0.396}Ti_{0.092}O_2$. Reprinted with permission from ref. 97 Copyright 2024, John Wiley and Sons.

by enhancing the participation of anionic oxygen in charge compensation through the strategy of "pushing charge transfer on anions". Taking $Na[Li_{1/4}Ni_{1/3}Ru_{5/12}]O_2$ as an example, the comparative study shows that, compared with the Ni redox-dominated system, the samples enhanced with anionic redox have significantly reduced the changes of the *a*- and *c*-axis during the charging and discharging process, and the multiple phase transitions of O3–P3–O1 have been suppressed significantly.[94] And the *in situ* strain analysis reveals that the lattice microstrain changes are smaller and more uniformly distributed, which can be achieved at high rate and long cycling (Fig. 8a). This result suggests that the moderate introduction of stabilized anionic redox helps to reduce the Na-storage lattice strain under high-voltage, high-capacity operation. In high-voltage P2-type Na_xTMO_2, how to avoid O2 release and framework collapse while expanding the capacity by using anionic redox is another key issue. Zhao *et al.* proposed that by constructing gradient and de-clustered anionic redox centers in the TM layer, spatial de-clustering and radial gradient distribution of anionic redox can be achieved in the crystals, so that the anionic redox in the high-voltage region is spatially dispersed.[95] Notably, the resulting cathode delivered a reversible capacity of 247 mAh g^{-1} (20 mA g^{-1}) and maintained nearly zero lattice deformation during cycling ($\Delta a \approx 0.02\%$, $\Delta c \approx 0.54\%$, and cell-volume variation $\approx 0.5\%$) with solid-solution behavior and no detectable phase transitions. From the strain-crack perspective, it can be inferred that this de-clustering and gradient electronic structure design is conducive to reducing the cyclic stress concentration, thus weakening the driving force for crack initiation (Fig. 8b). To address the voltage decay of high-capacity oxygen-redox-active Na_xTMO_2, Zhang *et al.* found that the voltage decay is closely related to the spatial inhomogeneity of the local Mn redox and the accompanying structural distortion by systematically analyzing the local structural evolution of the lattice oxygens involved in the redox process.[96] Weakening the Mn–O covalency by strong Al–O bonding can significantly suppress the voltage decay and maintain the integrity of the lattice framework (Fig. 8c and d). Such studies reveal how irrational anionic redox induces structural fatigue with potential crack sources at the electronic structure level, and give specific methods for crack-resistant design at the electronic level by modulating the nature of TM–O bonds. Furthermore, Li *et al.*'s systematic work around coordination chemical–electronic structures shows that by regulating the degree of

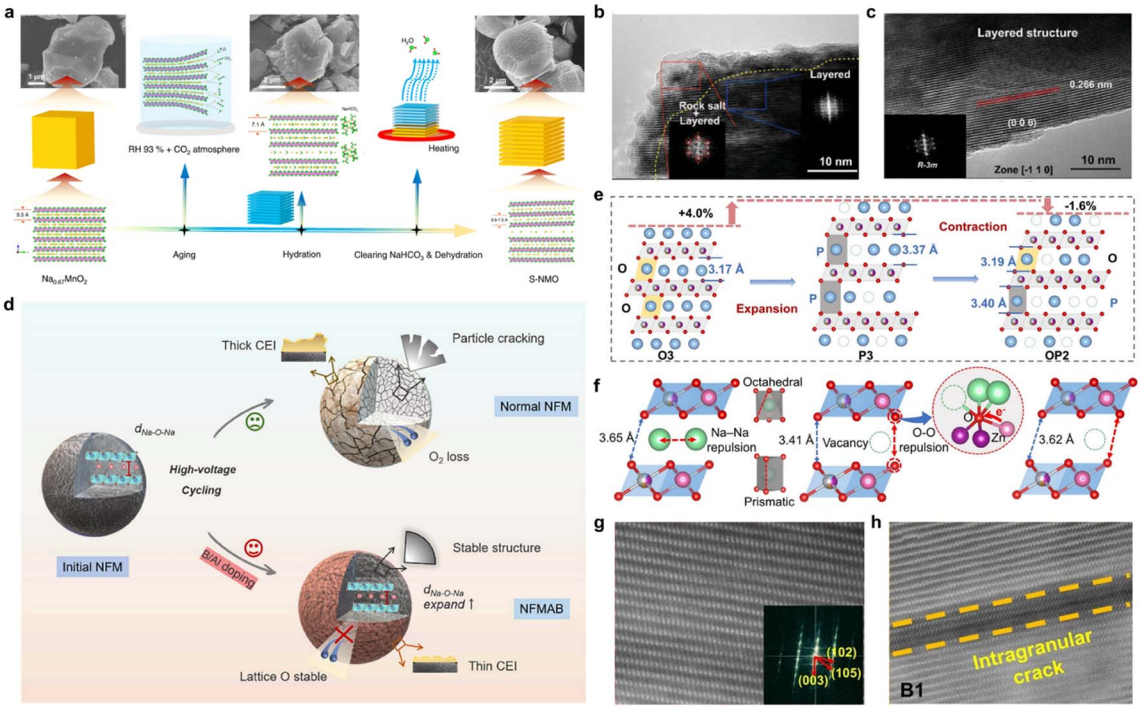

Fig. 9 (a) Schematic illustration of the preparation process of shale-like Na_xMnO_2. Reprinted with permission from ref. 104 Copyright 2021, Springer Nature. The HRTEM images of (b) O3–$Na_{0.8}Ni_{0.4}Fe_{0.2}Mn_{0.4}O_2$ and (c) $Na_{0.8}Ni_{0.3}Fe_{0.2}Mn_{0.3}Li_{0.1}Mg_{0.02}Ca_{0.05}Sb_{0.03}O_2$. Reprinted with permission from ref. 105 Copyright 2023, John Wiley and Sons. (d) Schematic diagram of B and Al co-doping O3–$NaNi_{1/3}Fe_{1/3}Mn_{1/3}O_2$ to stabilize phase transitions and lattice oxygen. Reprinted with permission from ref. 106 Copyright 2025, John Wiley and Sons. (e) Schematic diagram of structural changes in $Na_{0.9}Ni_{0.32}Zn_{0.08}Fe_{0.1}Mn_{0.3}Ti_{0.2}O_2$ and (f) O–O length and repulsion changes of $Na_{0.9}Ni_{0.32}Zn_{0.08}Fe_{0.1}Mn_{0.3}Ti_{0.2}O_2$ during Na^+ extraction; HAADF-STEM image of (g) $Na_{0.9}Ni_{0.32}Zn_{0.08}Fe_{0.1}Mn_{0.3}Ti_{0.2}O_2$ and (h) $Na_{0.9}Ni_{0.4}Fe_{0.1}Mn_{0.5}O_2$ after 400 cycles. Reprinted with permission from ref. 107 Copyright 2024, John Wiley and Sons.

distortion and the connection mode of the TM–O polyhedral, the anisotropic lattice strain can be significantly reduced and the reversibility of structural evolution can be enhanced while ensuring the continuity of Na^+ migration channels. This class of materials exhibits small volume changes with good structural reversibility over a wide potential window, indirectly suggesting that structural toughness can be provided for microcrack suppression through coordination chemical–electronic structure synergistic design (Fig. 8e–h).[97] Correspondingly, the cycled particles remain crack-free and TM migration, and the KT-NFM||HC pouch cell maintains >90% capacity retention after 2000 cycles while delivering a reversible capacity of 138.6 mAh g^{-1} and an energy density of 135.6 Wh kg^{-1}. From an electronic-structure standpoint, stabilizing anionic redox and delocalizing O-2p states help convert highly localized O-redox, which is associated with strong local volume contraction and stiffness increase, into a more spatially homogeneous redox process. *In situ* strain mapping and spectroscopic imaging reveal that such designs significantly flatten the gradients of local valence state and chemical strain, thereby lowering the peak stress at interfaces and suppressing the initiation of microcracks along these regions.

Taken together, compositional and electronic structure modulation not only alters the average structural stability through Na/TM ratio, doping, and high-entropy configurations, but also establishes a favorable synergistic relationship between the electronic structure and lattice strain by modulating the charge compensation mode and coordination chemistry. The design around low strain window and controllable anionic redox enables the Na_xTMO_2 to maintain low internal stress and limited structural damage even at high specific capacity and high operating voltage, thus suppressing the generation and accumulation of microcracks at the intrinsic level, and providing a solid foundation for the subsequent structural and interfacial engineering strategies.[101–103]

3.2 Strain and phase engineering

Under defined electronic structure conditions, phase transition paths and lattice strains are a direct source of microcrack evolution. The compositional strategies discussed in the previous section largely define the accessible phase space, whereas the present section focuses on how to explicitly regulate the spatial distribution and accumulation of chemo-mechanical strain through structural design at both the crystallographic and particle levels. The evolution of Na_xTMO_2 in multiphase intervals such as O3/P3/OP2 or P2/O2/OP4 is commonly accompanied by pronounced *c*-axis contraction and anisotropic lattice distortion. If these strains are not homogeneous in time and space, stress concentrations and crack initiation can be induced inside the grains, at phase boundaries, or along internal grain boundaries in secondary particles.[40,108] In this section, we discuss how to weaken

the driving force of microcracks at the structural level through low-strain phase-path design, negative-expansion or near-zero-strain structures, heterogeneous/gradient architecture, and more recently, single-crystal particle design that reduces grain-boundary-mediated stress accumulation and crack-initiation sites.[109–111]

The ratio of Na layer spacing to TM layer spacing has a direct effect on the phase transition path and volumetric strain.[112] Yang *et al.* constructed shale-like Mn-based P2-type layered oxides by water-mediated treatment as an example, and significantly enlarged the Na^+ layer spacing, which can achieve a near-zero strain structure with almost zero volumetric change during the charge/discharge process.[104] *In situ* XRD and strain analyses show that these materials can maintain a stable P2 structure under long cycling and high rate conditions, and macroscopically exhibit ultra-long lifetimes and excellent rate performance (Fig. 9a). This type of "Na-layer spacing engineering" essentially involves geometrically shrinking the *a*/*b* planes and expanding the *c*-axis to compensate for each other at the bulk scale, thus significantly reducing the driving force for microcrack initiation. In the high-voltage O3-type system, multiple doping and high-entropy configurations are used to modulate the multiphase evolutionary paths such as O3–P3–OP2 and their accompanying volume changes, thereby moderating the accumulation of stresses associated with the phase transitions. Xia *et al.* used the O3–$Na_{0.8}Ni_{0.3}Fe_{0.2}Mn_{0.3}Li_{0.1}Mg_{0.02}Ca_{0.05}Sb_{0.03}O_2$ as a representative example and showed that the synergistic doping of multiple cations can significantly suppress the harmful phase transition and irreversible structural rearrangement above 4.1 V, so that the O3 framework still maintains a better structural reversibility in the high-voltage region, the volume change is compressed, and the structural degradation during cycling is delayed (Fig. 9b and c).[105] *In situ* XRD further shows a reduced 003 peak shift ($\Delta 2\theta \approx 0.24°$ *vs.* 0.53°) and a smaller *c*-axis variation ($\Delta c \approx 1.2337$ Å *vs.* 1.5493 Å), consistent with an improved capacity retention of 85.0% after 250 cycles (*vs.* 67.2% for the undoped counterpart). Similarly, Sun *et al.* enhanced the framework stiffness and stabilized the lattice oxygen by employing Al and B double doping in O3–$NaNi_{1/3}Fe_{1/3}Mn_{1/3}O_2$, using the strong covalent bonding of Al–O and B–O. This significantly moderated the O3–P3–OP2 multiphase evolution associated with the bulk strain and structural irreversibility (Fig. 9d).[106] Furthermore, more extreme "strain compensation" at the bulk scale can be achieved by constructing O3-type Na_xTMO_2 with negative expansion behavior.[113] Li *et al.* introduced Zn/Ti co-doping in the O3–$Na_{0.9}Ni_{0.4}Fe_{0.1}Mn_{0.5}O_2$ system, which produces a non-monotonic *c*-axis response (*c* expands by ~3.7% upon charging and then contracts by ~1.7%), leading to a much smaller net Δc (~2.0% *vs.* ~5.0% in the parent) and substantially reduced interslab/volume changes (2.4%/1.9% and 5.2%/9.8%) (Fig. 9e and f). The post-cycling multiscale characterization shows that the material maintains good structural reversibility at high voltage and long cycling, reflecting the potential of the negative expansion design in suppressing structural destabilization (Fig. 9g).[107] High-entropy O3-type Na_xTMO_2 extends the low-strain design to the in-plane scale from another perspective. Hu *et al.* have constructed O3–$NaNi_{0.3}Cu_{0.1}Fe_{0.2}Mn_{0.3}Ti_{0.1}O_2$ and its Sn^{4+} substitution comparison system $NaNi_{0.3}Cu_{0.1}Fe_{0.2}Mn_{0.3}Sn_{0.1}O_2$. The systematic analysis shows that the former has a smaller and more uniform in-plane strain during charging and discharging, and its structural reversibility and cycling stability are significantly better than that of the latter (Fig. 10a and b). The maximum planar strain is reduced from 2.38% to 0.51% on charge and from 3.43% to 0.93% on discharge. O3–$NaNi_{0.3}Cu_{0.1}Fe_{0.2}Mn_{0.3}Ti_{0.1}O_2$ shows a reversible capacity of 120 mAh g^{-1} at 5C with 86% capacity retention after 500 cycles, compared to 76 mAh g^{-1} capacity and 59% capacity retention for $NaNi_{0.3}Cu_{0.1}Fe_{0.2}Mn_{0.3}Sn_{0.1}O_2$. Combining *in situ* diffraction and strain analysis, it is clearly pointed out that planar strain is a key indicator affecting the stability of high-entropy layered oxide structures, and a more favorable planar stress state can be obtained by reasonably selecting high-entropy components, thus attenuating the driving force of microcrack sprouting and expansion (Fig. 10c–f).[114] On this basis, the effect of high entropy modulation on the O–P phase transition path and anion behavior was further revealed by the entropy-tailored design of the O3–$NaNi_{0.3}Fe_{0.4}Mn_{0.3}O_2$ system. Amine *et al.* constructed a high entropy solid solution by introducing a variety of chemically compatible elements, such as Cu, Co, Ti, *etc.*, to the TM layer, and the high entropy samples were found in the O3 region. The high-entropy samples exhibited greater lattice parameter changes in the O3 region, but the duration of the O–P biphasic region was significantly shortened. In addition, the Na^+ diffusion kinetics and

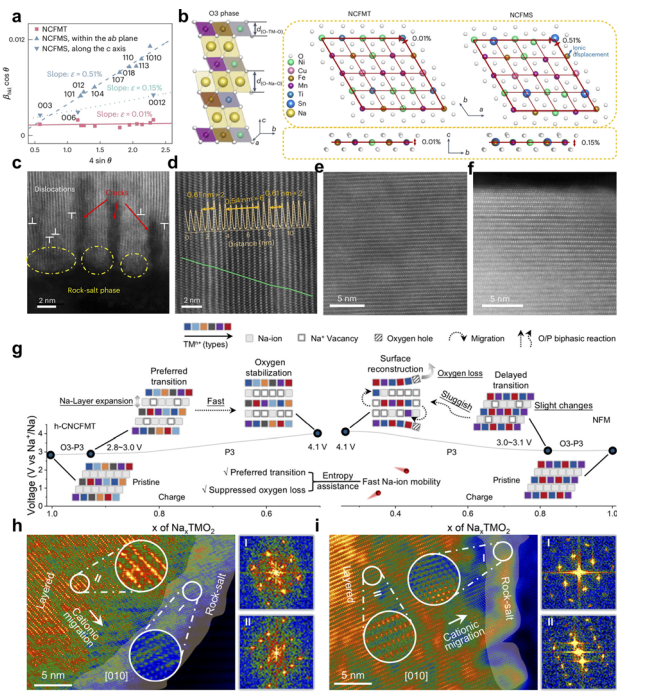

Fig. 10 (a) Evaluating the anisotropic strain distribution of electrode materials *via* the Williamson–Hall method. (b) Schematic diagrams of O3–$NaNi_{0.3}Cu_{0.1}Fe_{0.2}Mn_{0.3}Ti_{0.1}O_2$ and O3–$NaNi_{0.3}Cu_{0.1}Fe_{0.2}Mn_{0.3}Sn_{0.1}O_2$ structures; HAADF-STEM images after cycling: (c and d) O3–$NaNi_{0.3}Cu_{0.1}Fe_{0.2}Mn_{0.3}Sn_{0.1}O_2$, (e and f) O3–$NaNi_{0.3}Cu_{0.1}Fe_{0.2}Mn_{0.3}Ti_{0.1}O_2$. Reprinted with permission from ref. 114 Copyright 2024, Springer Nature. (g) Schematic of the structural evolution of $NaNi_{0.3}Fe_{0.4}Mn_{0.3}O_2$ and $NaCu_{0.1}Ni_{0.2}Co_{0.2}Fe_{0.2}Mn_{0.15}Ti_{0.15}O_2$ during charging and discharging processes; HAADF-STEM images after cycling: (h) $NaNi_{0.3}Fe_{0.4}Mn_{0.3}O_2$, (i) $NaCu_{0.1}Ni_{0.2}Co_{0.2}Fe_{0.2}Mn_{0.15}Ti_{0.15}O_2$. Reprinted with permission from ref. 115 Copyright 2025, American Chemical Society.

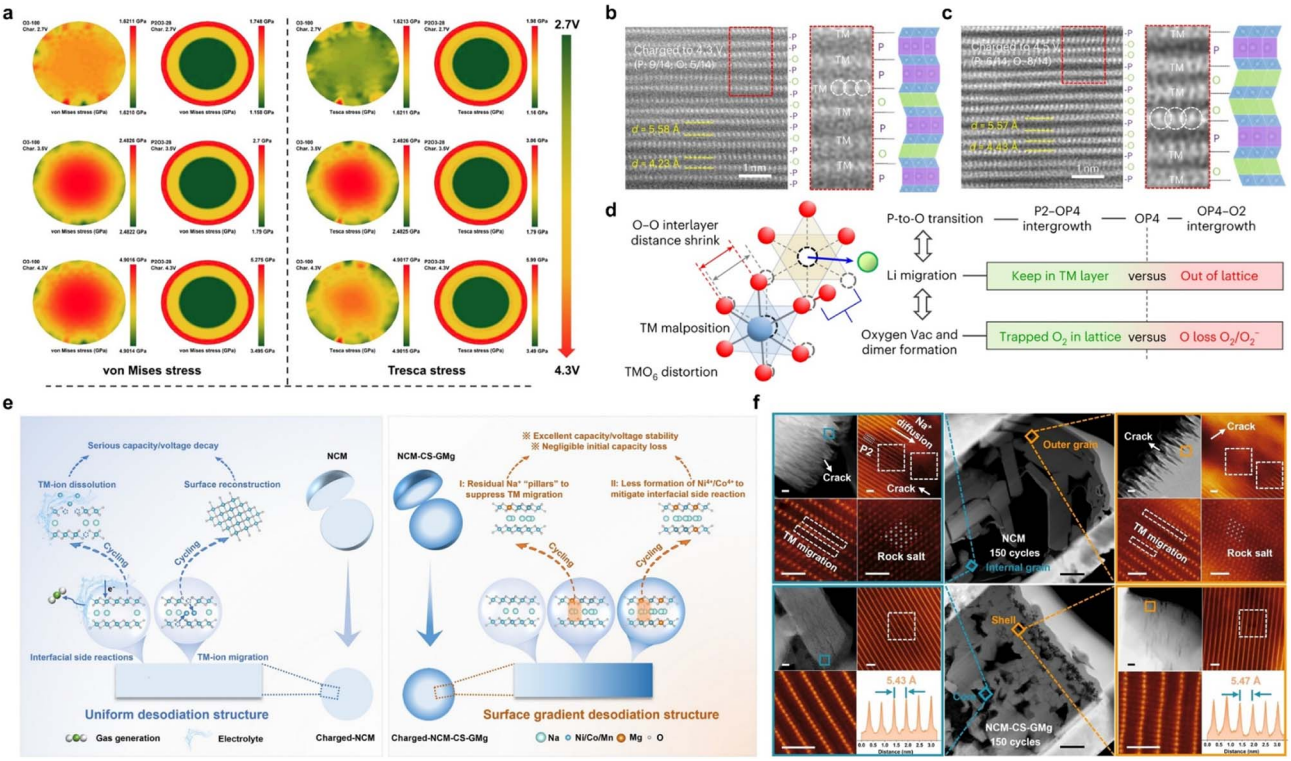

Fig. 11 (a) Finite element-based mechanical stress simulation results.[118] Copyright 2025, John Wiley and Sons. HAADF-STEM images of P2–$Na_{0.67}Li_{0.1}Fe_{0.37}Mn_{0.53}O_2$ at different charge states: (b) 4.3 V, (c) 4.5 V; (d) schematic of LiO_6/TMO_6 distortion in the charged P2–$Na_{0.67}Li_{0.1}Fe_{0.37}Mn_{0.53}O_2$ structure viewed along the (001) direction. Reprinted with permission from ref. 119 Copyright 2024, Springer Nature. (e) Schematic diagram illustrating the degradation mechanism of P2–$Na_{0.72}Ni_{0.2}Co_{0.25}Mn_{0.55}O_2$ and the surface gradient desodiation structure design concept for P2–$Na_{0.72}Ni_{0.20}Co_{0.21}Mn_{0.55}Mg_{0.036}O_2$ materials; (f) structural and valence state evolution of P2–$Na_{0.72}Ni_{0.2}Co_{0.25}Mn_{0.55}O_2$ and P2–$Na_{0.72}Ni_{0.20}Co_{0.21}Mn_{0.55}Mg_{0.036}O_2$ cathodes after 150 cycles. Reprinted with permission from ref. 120 Copyright 2024, John Wiley and Sons.

high rate performance were significantly improved, while the irreversible oxygen loss and TM migration during deep desodiation were effectively suppressed, and the surface structural remodeling was significantly weakened (Fig. 10g–i).[115] Similarly, the multidoping work for zero-Li and zero-Co Na_xTMO_2 shows that the synergistic introduction of multiple aliovalent cations into the TM octahedral sites effectively slows down the lattice strain accumulation during cycling, enhances the oxygen stability, and reduces the magnitude of the volume change, thus suppressing the near-surface structural deconstruction, interfacial side-reactions, and the formation of microcracks.[116] These high-entropy and multication designs together give a pathway from in-plane strain, volume vibration to interface chemistry synergistic optimization, enabling high-voltage Na_xTMO_2 to maintain more robust structural stability while obtaining high energy density and fast-charging capability, which provides an important complement at the structural level for microcrack suppression.[117]

From the above results, it can be seen that whether the near-zero-strain structure is constructed by using Na-layer spacing engineering, or the O3/P3/OP2 phase diagram and planar strain are adjusted by multidoping and high-entropy configuration, the core idea is to transform the strain originally concentrated at a specific phase transition point or crystallographic direction into a spatially more homogeneous and amplitude-small structural response, thus suppressing the microcrack formation at the structural level.[121] In addition, the utilization of heterogeneous structures and structural gradients to achieve stress redistribution within particles has also been one of the important directions in recent years to mitigate microcrack-related failures.[122] Recently, Xiao *et al.* took the construction of the P2/O3 heterostructure cathode as an example. By constructing a radial two-phase structure of O3 core and P2 shell within a single particle, the difference in structural evolution behavior and mechanical response between the P2 shell layer and the O3 core can be exploited, so that the shell layer can participate in and share the stresses of the O3 phase at high voltage. Experimental characterization and finite element simulations show that this P2/O3 heterostructure exhibits higher capacity retention and more moderate plastic deformation than a single O3 material under high-voltage long cycling, and the overall structural stability is significantly improved (Fig. 11a).[118] From the microcracking perspective, the P2 shell layer is equivalent to providing a mechanical buffer for the O3 core, which helps to reduce the risk of localized strain concentration within the single phase. Multiphase and heterogeneous structures can also emerge in more complex multilayer designs. Qiao *et al.*'s study of P2–$Na_{0.67}Li_{0.1}Fe_{0.37}Mn_{0.53}O_2$ materials showed that deep desodiation induces the formation

of layer dislocations in the neighboring O-type stacks, giving rise to a P/O intergrowth structure (Fig. 11b and c). The ordered OP4 phase obtained at 4.3 V SoC ($Na_{0.26}$) can be regarded as the boundary between the P2–OP4 and OP4–O2 transitions. In this regard, the combined state of P-type and O-type stacking can be controlled to form a more favorable coupling between the laminar stacking evolution and the anionic redox process, thus maintaining high voltage stability while keeping high reversible capacity and realizing pouch batteries with high energy density (270 Wh kg^{-1}, 1.5–4.3 V). This suggests that the structural strain associated with the phase transition can be moderated without disrupting the overall layered skeleton by introducing moderate P/O layer dislocations and intergrowth inside the crystal (Fig. 11d).[119] The surface gradient structure provides a means of easing stress and suppressing surface structural degradation along the shell–core direction of the particles. In P2-$Na_{0.72}Ni_{0.2}Co_{0.25}Mn_{0.55}O_2$, Zhang *et al.* constructed a gradient cation distribution by enriching Mg in the near-surface region. Thereby, a certain amount of Na^+ pillars can be retained in the surface layer after high-voltage desodiation, thus suppressing excessive desodiation-induced TM migration and layered-rock salt phase transition. Deep-resolution structural and chemical analyses show that this surface gradient desodiation design significantly reduces the structural remodeling and microcracks on the particle surface, which is conducive to maintaining a more coordinated structural evolution between the shell and the core during long cycling (Fig. 11e and f).[120] In addition, Xiang *et al.* reported that ultrafast lattice engineering using nonequilibrium high temperature shock (HTS) treatment can reconstruct the defects and local structures of layered oxides in a short time. In the $Na_{0.67}MnO_2$ system, the HTS treatment can suppress the Mn vacancies in the TM layer, increase the sites that can participate in the redox and modulate the Mn 3d orbital energy levels, and also controllably introduce the transition metal layer stacking faults, which attenuates structural transformation and Na^+/vacancy ordering during cycling. The treated materials are significantly better than the conventional solid-phase synthesized samples in terms of energy density, rate performance, and cycling stability, suggesting that optimization of the defect structure through nonequilibrium lattice engineering can mitigate structural fatigue without changing the topology of the layered skeleton.[127] From a microcracking perspective, the above designs, although having different focuses, still share a common feature: instead of simply pursuing the minimization of the overall volume change, the stresses associated with phase transitions are spatially dispersed and moderated by carefully arranging regions within the particles with different structural responses. This mechanism of strain redistribution is expected to increase the crack initiation threshold and reduce the probability of cracks running through the particles along a single path, providing a new structural design idea for microcrack suppression in high-voltage, high-capacity Na_xTMO_2.

Beyond stress redistribution through heterostructure coupling and surface-gradient regulation, reducing crack-initiation sites at the particle level has also emerged as an effective strategy. In conventional polycrystalline layered oxides, grain boundaries are natural locations for anisotropic strain accumulation, intergranular separation, and subsequent electrolyte penetration. In this context, single-crystal or quasi-single-crystal layered oxides have recently attracted increasing attention because they can suppress grain-boundary-related cracking while simultaneously reducing the surface exposed to electrolyte and humid air. Recent studies on O3-type sodium layered oxides show that this design can moderate lattice deformation, alleviate interfacial parasitic reactions, and improve long-term structural integrity under high-voltage cycling. For example, single-crystal O3–$Na[Ni_{0.3}Mn_{0.35}Cu_{0.1}Ti_{0.25}]O_2$ exhibited clearly improved durability, retaining 84.4% of its capacity after 200 cycles at 0.5C, and its corresponding full cell still maintained 81.5% capacity retention after 1000 cycles at 2C, reflecting the benefit of reducing grain-boundary-mediated degradation.[128] In parallel, the grain-boundary-free O3–$Na[Ni_{0.3}Mn_{0.5}Cu_{0.1}Ti_{0.1}]O_2$ further demonstrates that stabilizing the exposed crystal surface can simultaneously suppress interlayer sliding and interfacial degradation under high voltage, while single-crystalline $Na[Ni_{1/3}Fe_{1/3}Mn_{1/3}]_{0.9}Cu_{0.05}Ti_{0.05}O_2$ in the commercially relevant O3-NFM system shows substantially reduced intergranular cracking together with improved cycling and moisture stability.[129,130] These results suggest that the main advantage of single-crystal design lies not simply in eliminating grain boundaries, but in weakening the coupled pathway of stress concentration, crack formation, and crack-assisted chemical attack. Nevertheless, single crystallization should not be viewed as a universal solution, because excessively long diffusion pathways or insufficient bulk structural regulation may still lead to reaction heterogeneity and intragranular damage. Therefore, for sodium layered oxides, a more promising direction may be to combine single-crystal particle architecture with additional phase/bonding engineering to achieve both crack resistance and reaction homogeneity.[131]

3.3 Interphase engineering for crack tolerance

Under high voltage and long cycling conditions, Na_xTMO_2 commonly faces electrolyte erosion, surface lattice remodeling, transition metal dissolution, and the resulting induced stress concentration and microcrack propagation. The coating helps mitigate structural–mechanical failure by modulating interfacial chemistry, charge and ion transport, and the mechanical boundary conditions of the surface layer. Therefore, increasing the material threshold for cracking and weakening the positive feedback between cracking and interfacial corrosion by optimizing the interfacial layer properties from the particle and electrode level is the third key dimension for achieving long-life Na_xTMO_2.[132]

Oxide-based interfacial layers, including simple metal oxides, mixed oxides, perovskite-type oxides, and layered/tunnel-type oxide shell layers, represent one of the earliest and most systematically studied classes of interphase engineering tools for suppressing surface degradation and crack propagation in Na_xTMO_2.[133,134] In general, these coatings can achieve the purpose of inhibiting the erosion of corrosive

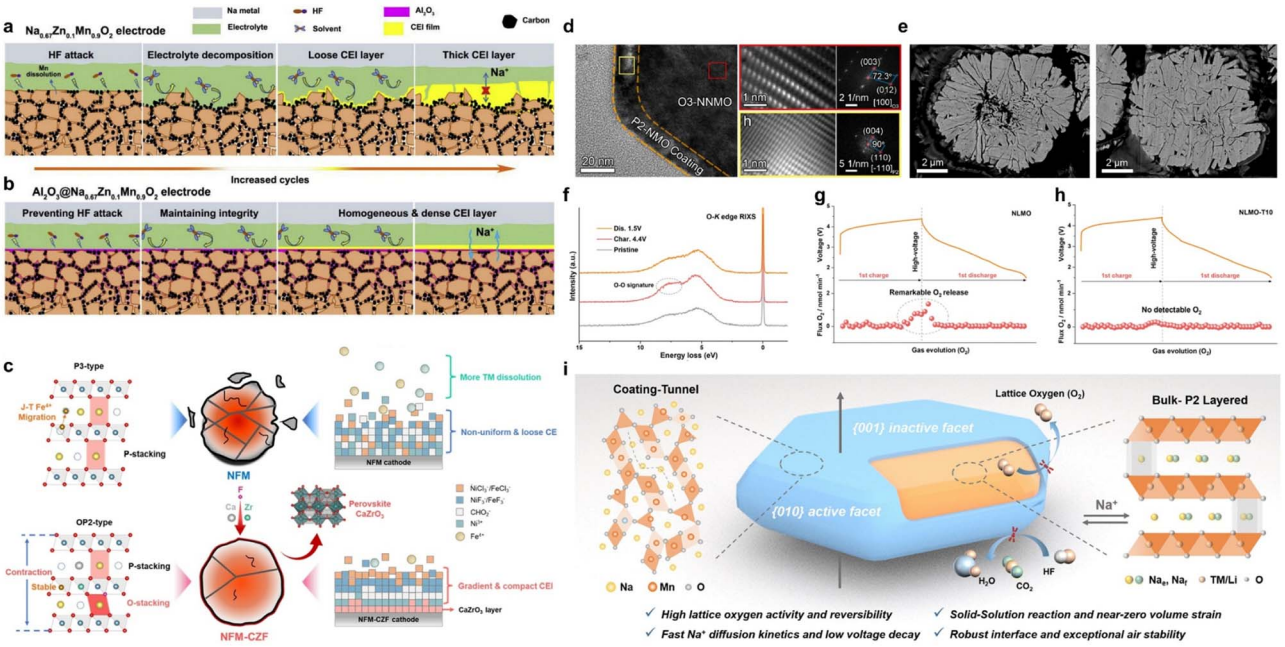

Fig. 12 Schematic illustration of the surficial evolutions of (a) $Na_{0.67}Zn_{0.1}Mn_{0.9}O_2$ and (b) Al_2O_3@$Na_{0.67}Zn_{0.1}Mn_{0.9}O_2$ electrodes. Reprinted with permission from ref. 123 Copyright 2020, Elsevier. (c) Schematic illustration of the structural evolution and modification mechanisms of O3–$NaNi_{1/3}Fe_{1/3}Mn_{1/3}O_2$ and O3–$NaNi_{1/3}Fe_{1/3}Mn_{1/3}O_2$@$CaZrO_3$ during electrochemical cycling. Reprinted with permission from ref. 124 Copyright 2025, John Wiley and Sons. (d) HRTEM image alongside their corresponding fast Fourier transforms of O3–$NaNi_{0.5}Mn_{0.5}O_2$@5% P2–$Na_{2/3}MnO_2$; (e) SEM images after 200 cycles of O3–$NaNi_{0.5}Mn_{0.5}O_2$ and O3–$NaNi_{0.5}Mn_{0.5}O_2$@5% P2–$Na_{2/3}MnO_2$. Reprinted with permission from ref. 125 Copyright 2022, Elsevier. (f) RIXS spectra of $Na_{0.75}Li_{0.25}Mn_{0.75}O_2$@10mol% $Na_{0.44}MnO_2$ under different charge–discharge states, along with *in situ* DEMS results of (g) $Na_{0.75}Li_{0.25}Mn_{0.75}O_2$ and (h) $Na_{0.75}Li_{0.25}Mn_{0.75}O_2$@10mol% $Na_{0.44}MnO_2$ during the first cycle; (i) schematic diagram of the mechanism for multifunctional tunnel structure modification. Reprinted with permission from ref. 126 Copyright 2025, Royal Society of Chemistry.

species such as HF, slowing down the lattice remodeling, promoting the migration of Na^+, improving the thermal stability, and assuming the role of the stress buffer layer between the bulk phase and the electrolyte to a certain extent, by constructing a dense, continuous and chemically stable protective layer on the particle surface.[135] Among the general oxide coatings, Al_2O_3 coating is one of the most typical representatives. Yang *et al.* utilized atomic layer deposition to construct a uniform Al_2O_3 coating on the surface of $Na_{0.67}Zn_{0.1}Mn_{0.9}O_2$ to form a CEI layer with uniform composition and dense structure, which significantly inhibited further decomposition of the organic electrolyte and accumulation of fluorine-containing by-products.[123] This results in a flat and continuous surface topography of the cathode after long cycling while increasing the coulombic efficiency of the material and decreasing the interfacial impedance (Fig. 12a and b). The optimized material maintained 83% capacity after 100 cycles at a current density of 12 mA g^{-1}. Similarly, Liu *et al.* found that the TiO_2 coating could also inhibit the particle surface side reactions and maintain the structural integrity after the simultaneous introduction of Ti doping with TiO_2 surface coating in O3–$NaNi_{0.33}Fe_{0.33}Mn_{0.33}O_2$. Accompanied by Ti^{4+} doping, it not only enlarges the Na layer spacing and improves the Na^+ diffusion kinetics, but also simultaneously reduces the Mn^{3+} content, attenuates the Jahn–Teller distortion, and integrally enhances the stability of the lamellar skeleton.[136] Similarly, Xu *et al.* reported that combining bulk Al doping with a surface ZnO coating in P2-$Na_{2/3}Ni_{1/3}Mn_{2/3}O_2$ effectively alleviated lattice stress and suppressed interfacial side reactions during cycling.[137] After long cycling, the coated samples showed more complete particle profiles and significantly fewer surface cracks. In such coating systems, the coating mainly weakens electrolyte decomposition and TM dissolution. And by improving the interface electron/ion transmission network, the body stress can be released more uniformly, which helps to reduce the risk of crack propagation caused by local stress concentration at the surface. In addition to this, more complex oxide interfacial layers include perovskite-type coatings, among others.[133,138–140] For example, Ji *et al.* introduced Ca, Zr, and F multisite doping in the O3–$NaNi_{1/3}Fe_{1/3}Mn_{1/3}O_2$ bulk phase and constructed a $CaZrO_3$ perovskite-type interfacial layer on the particle surface, which can realize synergistic reinforcement from the atomic scale to the particle scale. Structural and morphological characterization shows that the $CaZrO_3$ shell layer remains continuous and dense after high-voltage cycling, significantly reducing surface lattice distortion and interface shear strain, and after cycling, the particle surface changes from the previous blocky fragmentation to a flatter interface morphology (Fig. 12c).[124] Electrochemically, the polarization after 100 cycles is markedly reduced ($\Delta E \approx 200$ mV *vs.* 557.2 mV), and the capacity retention at 2C can reach 83.80% after 300 cycles. This kind of perovskite coating with high modulus and chemical

stability is beneficial to buffer the stress generated by the phase transition of the bulk phase and retard the surface structural degradation process. There is another class of strategies for constructing lattice-matched oxide interfacial layers.[144,145] It mainly utilizes layered or tunneled oxides that are highly matched with the bulk crystal structure as the coating layer to synergistically regulate the phase transition, redox, and strain evolution behaviors at the interface, thus reducing the risk of structural degradation induced by non-uniform intercalation of Na^+.[146] Wei *et al.* constructed a P2/O3 core–shell structure by coating O3–$Na_{0.8}[Ni_{0.33}Mn_{0.67}]O_2$ with P2–$Na_{0.8}[Ni_{0.5}Co_{0.2}Mn_{0.3}]O_2$.[147] The P2 shell layer exhibits milder lattice parameter variations and phase transition behaviors in the high-voltage range, providing a lattice-matched buffer shell for the internal O3 core, thus protecting the core region. A similar structural design was demonstrated by Sun *et al.* who epitaxially grew a P2–$Na_{2/3}MnO_2$ shell layer of about 15 nm on the surface of O3–$NaNi_{0.5}Mn_{0.5}O_2$ to construct a highly lattice-matched layer–layer interface.[125] The P2 shell layer can provide stable Na^+ migration channels and a dense protective layer, reducing electrolyte erosion and surface structure reconfiguration, and also sharing part of the lattice distortion and volume change during multiple phase transitions, making the charge–discharge curve smoother and significantly improving cycle and rate performance. The characterization results showed that the surface degradation and particle pulverization degree of the coated samples were significantly reduced (Fig. 12d and e). Additionally, Xiao *et al.* constructed a $Na_{0.44}MnO_2$ tunnel phase coating on the surface of P2–$Na_{0.75}Li_{0.25}Mn_{0.75}O_2$, utilizing the excellent lattice matching of the tunnel structure with the layered bulk phase and three-dimensional channels. Under high-voltage anionic redox conditions, the lattice oxygen was stabilized by the tunnel interface. *In situ* XRD, resonant inelastic X-ray scattering (RIXS) and differential electrochemical mass spectrometry (DEMS), and stress simulations show that the tunnel interface can significantly suppress irreversible oxygen release and simplify the intrinsically complex multiphase transformation into a near-solid-solution-like evolution process. At the same time, it reduces stress peaks and local structural damage in the bulk phase, thereby attenuating the driving force for crack initiation and propagation arising from the coupling of anionic redox and phase transformation (Fig. 12f–i).[126] The capacity retention of the optimized material after 100 cycles at a current density of 0.2C is 91.24%, much higher than that of P2–$Na_{0.75}Li_{0.25}Mn_{0.75}O_2$, 23.33%, which verifies the effectiveness of the tunneling structure modification strategy in terms of electrochemical performance.

Fast ion conductors, especially $NaTi_2(PO_4)_3$ (NTP) and $NaMgPO_4$ with NASICON structure Na^+ conductors, due to their high Na^+ conductivity and excellent chemical stability, show unique advantages in Na_xTMO_2 interface engineering. First, such relatively rigid PO_4 tetrahedral skeletons are insensitive to redox-induced local structural distortions, which is conducive to maintaining a stable structural framework at the interface.[148] Secondly, these materials are Na^+ conductors themselves, which can act as a protective layer for the "a solid-electrolyte-like

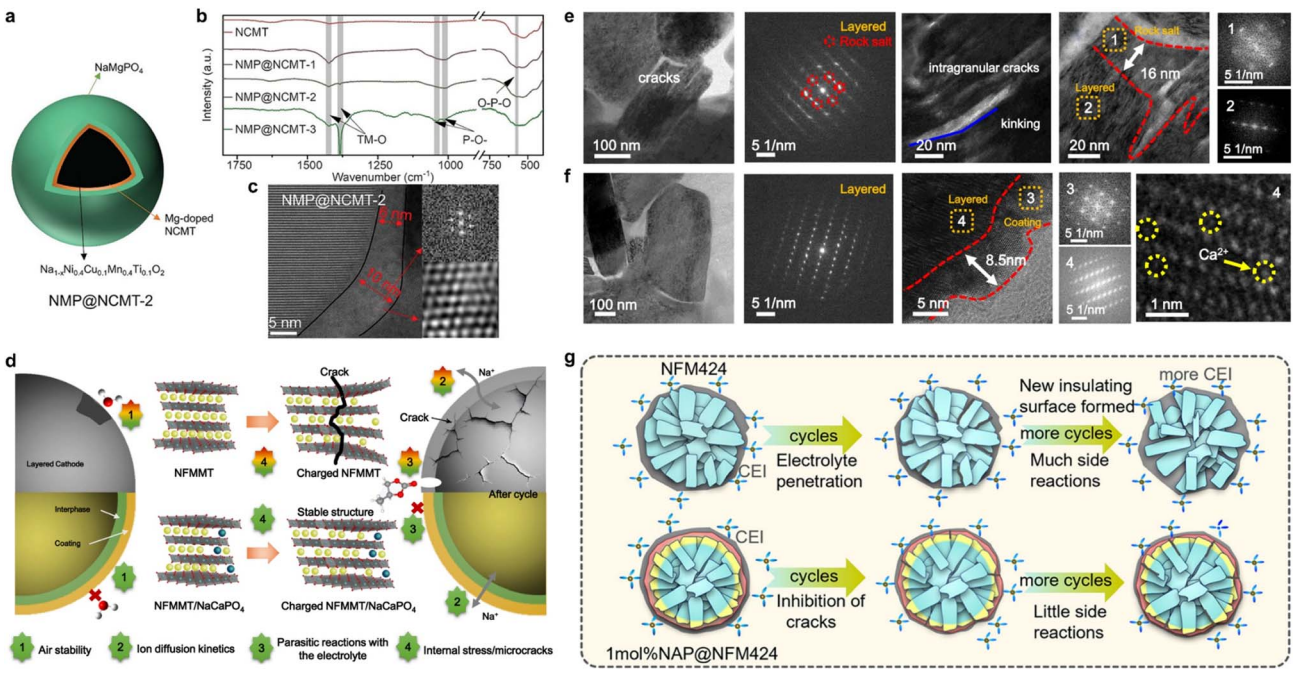

Fig. 13 (a) Schematic diagram of the structure of $NaMgPO_4$@$NaNi_{0.4}Cu_{0.1}Mn_{0.4}Ti_{0.1}O_2$-2, (b) infrared spectroscopy results and (c) STEM image. Reprinted with permission from ref. 141 Copyright 2023, John Wiley and Sons. (d) Schematic of a combined strategy enhancing structural stability through $NaCaPO_4$ coating and interphase Ca^{2+} concentration gradient doping; STEM and corresponding SAED results for (e) $Na[Ni_{0.4}Fe_{0.1}Mn_{0.4}Mg_{0.05}Ti_{0.05}]O_2$ and (f) $Na[Ni_{0.4}Fe_{0.1}Mn_{0.4}Mg_{0.05}Ti_{0.05}]O_2$@$NaCaPO_4$ after 200 cycles. Reprinted with permission from ref. 142 Copyright 2025, Springer Nature. (g) Schematic diagram of *in situ* formation of plastic crystals enhancing the comprehensive properties of materials. Reprinted with permission from ref. 143 Copyright 2023, American Chemical Society.

protective layer" without increasing the obvious diffusion resistance. Wang *et al.* formed a thin layer of NTP on the surface of P2–$Na_{0.67}Ni_{0.28}Mg_{0.05}Mn_{0.67}O_2$ by *in situ* coating. The NTP coating can effectively inhibit the structural collapse caused by the P2–O2 phase transition. Because NTP itself is a Na^+ conductor, the coating not only plays the role of a physical barrier, but also helps to maintain a relatively uniform Na^+ distribution during cycling, reducing the strain gradient due to localized Na-rich/poor regions.[149] Similarly, Liu *et al.* constructed NTP coatings on the P2–$Na_{0.65}Mn_{0.7}Ni_{0.16}Co_{0.14}O_2$ system using a similar strategy, and also observed that the phase transition was delayed, the structural stability was enhanced, and the long-cycling capacity decay was slowed down, which further supports the universality of the NASICON-type shell layer in terms of the interfacial stability of Na_x-TMO_2.[150] In addition to crystalline shell layers such as NTP, work on constructing $NaMgPO_4$ solid electrolyte layers using residual base conversion provides new ideas for interfacial engineering of ionic conductors. Hu *et al.* converted residual base $NaOH/Na_2CO_3$ on the surface to the $NaMgPO_4$ phase by reaction with a Mg source on an O3-type lamellar cathode (Fig. 13a), yielding a solid $NaMgPO_4$ layer with a thickness of around 8 nm and showing only a slight increase (to ~9 nm) after 100 cycles, while full cells were reported to run stably for over 300 cycles at 1.2C.[141] A protective layer rich in inorganic components with good Na^+ conductivity is formed on the particle surface. This interfacial layer can significantly reduce the side reaction between conventional residual alkali and electrolyte, reduce the thickness of non-conductive organic SEI, and at the same time provide rigid structural support for the surface layer, so that the volume change induced by the phase transition of the bulk phase is more uniformly transferred to the electrolyte side, which is conducive to avoiding the interfacial region from being a source of crack sprouting (Fig. 13b and c). $NaCaPO_4$ coatings are representative of a group of phosphate interfacial layers that are chemically stable and elementally regulated stabilization and elemental modulation.[151] In early studies, the high energy density O3 cathode surface was constructed with a $NaCaPO_4$ layer through a biomimetic strategy, which can significantly enhance the high-pressure cycling stability.[152] Recently, Sun *et al.* further constructed a $NaCaPO_4$ coating on O3–$NaNi_{1/3}Fe_{1/3}Mn_{1/3}O_2$ *via* a phosphate conversion reaction and realized the gradient introduction of Ca elements from the surface to the bulk phase (Fig. 13d).[142] This strategy improves the interface corrosion resistance, reduces electrolyte decomposition and TM dissolution, and optimizes the Na^+/TM arrangement and phase transition path in the bulk phase through Ca gradient doping, making the lattice parameter evolution during high-voltage cycling smoother. Overall, under the joint action of the $NaCaPO_4$ coating and the internal Ca doping, the volume anisotropy of the layered structure during the deep desodiation process is significantly reduced, and at the particle scale, it is manifested as a more complete surface morphology and fewer cracks in the secondary particle boundaries (Fig. 13e and f). Meanwhile, the cycling stability data also remain consistent with this stabilized interface: 81.0% capacity retention after 300 cycles at 0.5C, and even under a higher cutoff of 4.5 V a discharge capacity of 109.9 mAh g^{-1} with 71.2% retention after 150 cycles. It is worth noting that some phosphate interface layers also have the characteristics of both a solid electrolyte and flexible interface. In the research of Hu *et al.* on the *in situ* construction of plastic crystal $Na_{3-3x}Al_xPO_4$ coating, the plastic crystal shell provides high Na^+ conductivity while also having certain plasticity and self-regulation ability.[143] It can alleviate the local stress generated by the volume change in the bulk phase through structural rearrangement during the cycling process (Fig. 13g). This kind of "soft–rigid" interfacial layer is helpful to avoid new stress concentration at the interface due to the over-constriction of the rigid shell layer, thus improving the interfacial stability of the material. Overall, these fast ionic conductor coatings not only reduce the side reaction on the electrolyte side by introducing a structurally stable skeleton phase with good Na^+ conduction on the particle surface, but also provide a low-impedance Na^+ migration channel between the bulk phase and the interface, resulting in

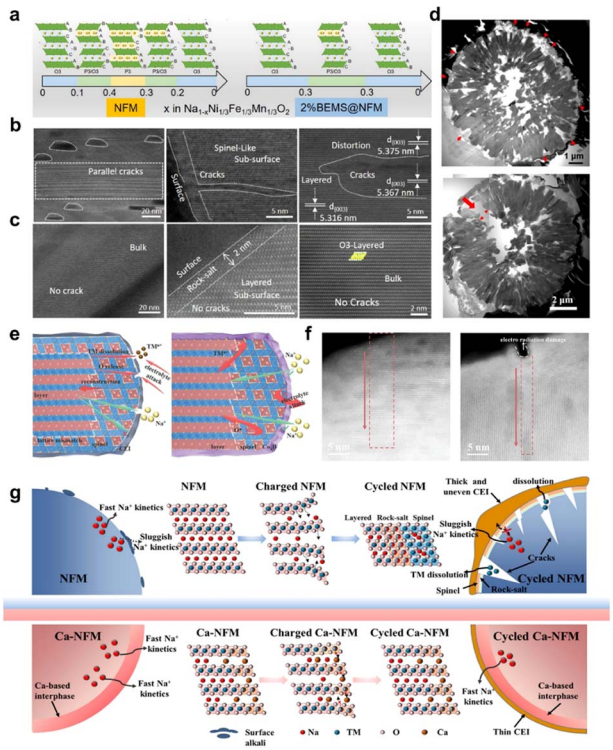

Fig. 14 (a) Phase structure evolution of 2% BEMS@$NaNi_{1/3}Fe_{1/3}Mn_{1/3}O_2$ during charging and discharging cycles; HAADF-STEM images for (b) O3–$NaNi_{1/3}Fe_{1/3}Mn_{1/3}O_2$ and (c) 2% BEMS@$NaNi_{1/3}Fe_{1/3}Mn_{1/3}O_2$. Reprinted with permission from ref. 153 Copyright 2025, Elsevier. (d) TEM cross-sectional images of O3–$NaNi_{0.65}Co_{0.08}Mn_{0.27}O_2$@$AlF_3$ and O3–$NaNi_{0.65}Co_{0.08}Mn_{0.27}O_2$ after 200 cycles. Reprinted with permission from ref. 154 Copyright 2018, American Chemical Society. (e) Schematic structural models and (f) HAADF-STEM images of O3–$NaNi_{1/3}Fe_{1/3}Mn_{1/3}O_2$ and 1 wt%-Co_xB@$NaNi_{1/3}Fe_{1/3}Mn_{1/3}O_2$. Reprinted with permission from ref. 155 Copyright 2024, John Wiley and Sons. (g) Schematic diagram of the structural evolution of $NaNi_{1/3}Fe_{1/3}Mn_{1/3}O_2$ and Ca–$NaNi_{1/3}Fe_{1/3}Mn_{1/3}O_2$. Reprinted with permission from ref. 156 Copyright 2025, American Chemical Society.

a more homogeneous stress release and a more controllable structural evolution in the process of intercalation, which is macroscopically manifested in the maintenance of better geometrical integrity and lower decay rate of the particles under the high-pressure and long-cycling.

In addition to oxides and fast ionic conductors, other inorganic coatings, such as fluorides, metal borides, and element-enriched interfacial layers, also show unique advantages in regulating interfacial chemistry, phase transition paths, and stress distribution.[79,99,157–159] By constructing interfacial layers with specific chemical functions or special mechanical properties, they inhibit high-pressure phase transitions, reduce interfacial side reactions and thermodynamic driving forces, and achieve the purpose of redistributing the strain between the bulk phase and the interface to a certain extent.[160] Fluoride interfacial layers usually play the roles of both HF-scavenging and modulation of phase transition pathways. Pan *et al.* achieved selective doping of elements such as Ca and Li as well as surface fluorination modification by the eutectic fluoride salt method in O3–$NaNi_{1/3}Fe_{1/3}Mn_{1/3}O_2$ (Fig. 14a).[153] Structural analysis shows that this strategy significantly reduces the cell volume change during the O3–P3 phase transition (cellularization decreases from 2.5% to 1.2% during charging and discharging) and forms a stable fluoride-enriched layer at the interface, which mitigates the structural and interfacial side-reactions at high pressures and rates. At a current density of 1C, the full battery achieves a capacity retention rate of 82% even after 1000 cycles. Smaller volume changes and more stable interfaces mean that the strain gradient between the interior of the grains and the surface layer is weakened, which is conducive to reducing the driving force for microcrack initiation and propagation during long cycling (Fig. 14b and c). Mullins *et al.* achieved the goal of protecting the internal gradient structure from rapid erosion by preferentially depleting the outer layer of AlF_3 against corrosive species, such as HF, during high-voltage cycling by forming an AlF_3 coating on the secondary particles of gradient Ni enriched O3–$NaNi_{0.65}Co_{0.08}Mn_{0.27}O_2$ nanorods[154] (Fig. 14d). Metal boride coatings have high electronic conductivity and excellent chemical stability, and when combined with oxide shell layers can form a bilayer interface with both chemical protection and a conductive "backbone". Wen *et al.* constructed a Co_xB-spinel bilayer coating *in situ*. The Co_xB in the inner layer of the coating provides a highly electronically conductive network, while the spinel coating in the outer layer assumes the roles of chemical protection and mechanical support (Fig. 14e).[155] This double-layer interface can significantly attenuate the surface lattice remodeling and TM dissolution after high-voltage cycling, allowing the cathode material to maintain a more intact surface structure. Meanwhile, due to the interface conductivity and mechanical support, the stress generated by the bulk phase transition can be more uniformly transferred to the electrolyte side, which helps to avoid localized crack initiation (Fig. 14f). Element-enriched interfacial layers, on the other hand, simultaneously regulate the phase transition path and interface chemistry by constructing a surface phase with a special crystal structure and an elemental gradient. Wang *et al.* introduced a Ca-enriched rock-salt shell layer and an internal Ca gradient doping on the surface of O3–$NaNi_{1/3}Fe_{1/3}Mn_{1/3}O_2$, which simplified the phase transition sequence during the high-voltage charging process and improved the corrosion resistance of the interface to the electrolyte at high voltages.[156] Multiple characterization studies show that this design can significantly attenuate the drastic phase transition like P3–OP2 and reduce the anisotropic strain in the crystals, which in turn reduces microcrack sprouting and connectivity inside and outside the secondary particles (Fig. 14g). Another type of multiphase "riveted" interfacial structures is characterized by the *in situ* generation of multiphase composite interfacial layers on the cathode surface.[161] This type of interfacial layer can inhibit the surface lattice slip and structural degradation through the interfacial pinning effect between multiphases, and at the same time, it also plays the role of "riveting" mechanically, so that the volume change of the bulk phase is more uniformly transferred to the surface layer. The combined results show that the structural integrity of the particle surface is significantly improved after high-pressure cycling, and the interface morphology is smoother, which is reflected in the reduction of the number of cracks and the restriction of expansion paths at the microcrack level. Overall, these inorganic boundary layers achieve multi-dimensional modulation from reaction thermodynamics to strain field distribution at the interface through specific chemical functions (HF trapping, phase transition simplification, elemental gradients, *etc.*) and special mechanical responses (highly conductive skeleton, multiphase pinning, sacrificial layer, *etc.*). Although the tolerance degree of microcracks varies among different systems, the general structural characterization results show that a reasonable interfacial layer design can maintain a more complete particle structure and interfacial morphology for the cathode material during high-pressure cycling, thus significantly delaying the capacity decay on a macroscopic scale, which provides a strong design guidance for understanding and suppressing the failure of layered cathodes caused by microcracks.

Although the above strategies act at different levels, they share a common purpose: to suppress microcrack initiation and propagation by reducing the driving force for structural damage or by interrupting the positive feedback between cracking and chemical degradation. To facilitate a more direct comparison across these approaches, Table 1 summarizes representative crack-mitigation strategies for layered oxide cathodes in sodium-ion batteries from the perspectives of strategy category, representative system, dominant crack scenario, key anti-cracking mechanism, electrochemical outcome, and practical limitation. This comparison is intended not as an exhaustive catalog of reported materials, but as a compact framework for clarifying the main design logic and applicability of different anti-cracking routes.

4 Summary and outlook

In summary, microcracking is a key factor in the structural degradation process of Na_xTMO_2 cathodes. In terms of the origin of microcracks, firstly, the stress accumulation triggered by the electrochemical reaction process is the most direct

Table 1 Representative crack-mitigation strategies, mechanisms, and electrochemical outcomes for layered oxide cathodes in sodium-ion batteries

Strategy	Material	Crack scenario	Anti-cracking mechanism	Capacity retention	Representative outcome
Electronic structure regulation	$Na_{0.7}Fe_{0.1}Mn_{0.75}\square_{0.15}O_2$ (ref. 85)	Phase-transition-induced bulk strain accumulation	Phase-transition suppression	70.1% (1C, 200 cycles)	Lower crack density and less pulverization
Electronic structure regulation	$Na_{2/3}Ni_{1/3}Mn_{2/3}O_2$ (ref. 86)	Phase-transition-induced bulk strain accumulation	Phase-transition suppression	85.8% (20C, 2500 cycles)	Delayed harmful phase transition
Electronic structure regulation	$Na_{7/9}[Li_{1/9}Ni_{1/9}Mg_{1/9}Mn_{6/9}]O_2$ (ref. 95)	Local stress concentration from redox/strain heterogeneity	Redox heterogeneity homogenization	91.4% (300 mA g^{-1}, 300 cycles)	Near-zero-deformation response
Electronic structure regulation	$Na_{0.8}Li_{0.24}Al_{0.03}Mn_{0.73}O_2$ (ref. 96)	Local stress concentration from redox/strain heterogeneity	Redox heterogeneity homogenization	98.8% (100 mA g^{-1}, 200 cycles)	Suppressed voltage decay
Electronic structure regulation	$Na_{0.898}K_{0.058}Ni_{0.396}Fe_{0.098}Mn_{0.396}Ti_{0.092}O_2$ (ref. 97)	Local stress concentration from redox/strain heterogeneity	Lattice-strain reduction	90.44% (200 mA g^{-1}, 2000 cycles)	Crack-free cycled particles
Strain and phase engineering	$Na_{0.8}Ni_{0.3}Fe_{0.2}Mn_{0.3}$-$Li_{0.1}Mg_{0.02}Ca_{0.05}Sb_{0.03}O_2$ (ref. 105)	Phase-transition-induced bulk strain accumulation	Phase-transition suppression	85% (2C, 250 cycles)	Improved high-voltage reversibility
Strain and phase engineering	$Na_{0.9}Ni_{0.32}Zn0._{08}Fe_{0.1}Mn_{0.3}Ti_{0.2}O_2$ (ref. 107)	Phase-transition-induced bulk strain accumulation	Lattice-strain reduction	93% (100 mA g^{-1}, 3600 cycles)	Reduced structural distortion
Strain and phase engineering	$Na_{0.67}Li_{0.1}Fe_{0.37}Mn_{0.53}O_2$ (ref. 119)	Phase-transition-induced bulk strain accumulation	Phase-transition suppression	92% (100 cycles)	Improved high-voltage stability
Strain and phase engineering	$Na_{0.72}Ni_{0.2}Co_{0.25}Mn_{0.55}O_2$ (ref. 120)	Grain-boundary/surface stress concentration	Stress redistribution	~63% (10C, 3000 cycles)	Reduced surface microcracks
Strain and phase engineering	$NaNi_{0.5}Mn_{0.5}O_2$@5% P2–$Na_{2/3}MnO_2$ (ref. 125)	Grain-boundary/surface stress concentration	Stress redistribution	83.6% (3C, 200 cycles)	More moderate particle deformation
Strain and phase engineering	$Na[Ni_{1/3}Fe_{1/3}Mn_{1/3}]_{0.9}Cu_{0.05}Ti_{0.05}O_2$ (ref. 130)	Grain-boundary/surface stress concentration	Stress redistribution	81.9% (0.5C, 300 cycles)	Better cycling and moisture stability
Interphase engineering	Al_2O_3@$Na_{0.67}Zn_{0.1}Mn_{0.9}O_2$ (ref. 123)	Interfacial corrosion-assisted cracking	Interfacial stabilization/ protection	83% (0.1C, 100 cycles)	Lower impedance and flatter surface
Interphase engineering	$NaNi_{1/3}Fe_{1/3}Mn_{1/3}O_2$@$CaZrO_3$ (ref. 124)	Interfacial corrosion-assisted cracking	Interfacial stabilization/ protection	83.8% (2C, 300 cycles)	Lower polarization and flatter interface
Interphase engineering	$Na_{0.75}Li_{0.25}Mn_{0.75}O_2$@$Na_{0.44}MnO_2$ (ref. 126)	Interfacial corrosion-assisted cracking	Interfacial stabilization/ protection	91.2% (0.2C, 100 cycles)	More solid-solution-like evolution
Interphase engineering	$Na_{0.67}Ni_{0.28}Mg_{0.05}Mn_{0.67}O_2$@NTP[149]	Interfacial corrosion-assisted cracking	Interfacial stabilization/ protection	77.4% (1C, 200 cycles)	Delayed phase transition
Interphase engineering	$NaMgPO_4$@$NaNi_{0.4}Cu_{0.1}Mn_{0.4}Ti_{0.1}O_2$ (ref. 141)	Interfacial corrosion-assisted cracking	Interfacial stabilization/ protection	70% (120 mA g^{-1}, 300 cycles)	Stable full-cell cycling over 300 cycles
Interphase engineering	$Na[Ni_{0.4}Fe_{0.1}Mn_{0.4}Mg_{0.05}Ti_{0.05}]$ O_2@$NaCaPO_4$ (ref. 142)	Interfacial corrosion-assisted cracking	Interfacial stabilization/ protection	82.9% (0.5C, 300 cycles)	Better post-cycling structural retention

causative factor. The deep intercalation of Na^+ leads to a series of phase transitions and interlayer slips, *etc.*, accompanied by anisotropic bulk and localized chemical stress field changes. When these internal stresses are unevenly distributed within the grains and exceed the local strength threshold of the material, microcracks sprout at phase boundaries or specific grain surfaces and gradually expand into a crack network through the grains. Secondly, environmental and interfacial factors greatly reduce the energy barrier for crack formation. Exposure of Na_xTMO_2 to humid air, CO_2, and electrolyte decomposition products tends to cause erosive reactions at the material interfaces, *e.g.*, when exposed to air, the Na^+/H^+ exchange reaction is prone to take place, which leads to the generation of residual bases such as sodium carbonate and sodium hydroxide. Transition metal ions such as Mn are easily dissolved when side reactions occur between the electrode and electrolyte during electrochemical processes. The mismatch between these corrosive phases and the internal body layered phases in terms of lattice parameters and elastic modulus leads to a significant increase in the interfacial residual stresses, thus lowering the threshold for crack initiation. Again, internal strains and defects during material synthesis likewise set the stage for microcracks. Precursor co-precipitation and sintering conditions may introduce microscopic defects such as dislocations and stacking faults, thereby leading to a pre-existing non-uniform stress distribution within the cathode particles. These defects are often inconspicuous during the initial cycle, but gradually evolve into crack sources after repeated charging and discharging, causing a structural collapse-type capacity drop after the material undergoes a short period of stabilization. Therefore, once formed, microcracks have a profound impact on the electrode performance, and can be considered as a key hub linking the intrinsic evolution of the material to the battery failure, both in terms of mechanical stress-driven internal particle fragmentation and chemical stress-driven interfacial side reactions.

To address the hazards of microcracks, various material design strategies have been proposed and validated, and the main idea is to reduce the generation of microcracks and minimize their effects at the countermeasure level. In addition to their effectiveness, however, the trade-offs and practical boundary conditions associated with these strategies also deserve explicit consideration, especially when translating crack-resistant design principles into high-energy-density and scalable cathode systems. (1) Composition and electronic structure regulation: modulate the bonding properties of the TM layer and oxygen layer through elemental doping or substitution to improve the intrinsic mechanical toughness and phase transition behavior of the material. For example, doping Mg^{2+}, Al^{3+}, *etc.* can enhance the TM–O bond strength and stabilize the lamellar skeleton, thus alleviating the lattice distortion during deep desodiation and reducing the tendency of structural cracking. Nevertheless, this route is often accompanied by non-negligible trade-offs, *e.g.*, excessive aliovalent doping may dilute redox-active species or perturb Na^+/vacancy ordering, which can manifest as compromised energy density or increased polarization in practical electrodes. High-entropy multidoping is also one of the extension strategies, which helps to reduce the anisotropic strain difference while increasing the structural disorder and modulating the anionic redox activity, contributing to the reduction of microcracks within the material after long cycling. However, the high-entropy benefit is not unconditional. The broadened local coordination distribution may complicate phase identification and mechanistic attribution, and in some compositions the elevated cation disorder can penalize Na^+ transport kinetics, making the balance between strain smoothing and rate capability/voltage hysteresis an important practical boundary condition. (2) Structural and lattice strain engineering: control the phase transition paths and strain magnitude through material structure design, and try to avoid drastic and localized volume changes. For example, the introduction of reversible transition phases (*e.g.*, OP4/Z phase) to replace the direct P2–O2 phase transition makes the evolution of lattice parameters more continuous and smoother, and significantly reduces the stress concentration at the phase boundary. As another example, a negative expansion component is constructed to counteract the interlayer shrinkage and realize a near-zero strain intercalation process. These structural optimization tools reduce the intensity of the stress source from the cell level, which reduces the driving force for microcrack initiation at the source. However, such structural and strain engineering strategies are not free of cost. Their effectiveness often depends on precise phase compatibility, interfacial coherence, and microstructural uniformity, while the associated synthesis complexity, compositional tolerance window, and scalability may impose practical constraints on their broader implementation. In some cases, the structural stabilization achieved through heterostructure construction or phase-path regulation may also be accompanied by trade-offs in tap density, voltage output, or processing reproducibility, which should be carefully balanced in practical cathode design. (3) Microstructure and interfacial engineering: starting from the particle and electrode level, the modulation of interfacial chemistry is used to improve the material's tolerance to cracks. A typical approach is to construct nanocoating or functional gradient shell layers on the cathode surface, such as inorganic protective layers of oxides, fast ionic conductors, and solid electrolytes. These coatings, on the one hand, isolate the active materials from direct contact with air and electrolyte to inhibit interfacial side reactions and harmful phase transitions, and on the other hand, act as an elastic cushion or skeleton support to redistribute the stress field on the particle surface. At the same time, coating strategies are inherently two-sided: overly thick/insulating layers may impede interfacial Na^+ transfer and amplify concentration polarization, whereas insufficiently robust layers can fracture or undergo chemical reconstruction during long cycling, turning into heterogeneous interfaces that accelerate crack-percolation and interfacial degradation. Therefore, coating chemistry, thickness uniformity, lattice/elastic matching, and scalable manufacturability must be co-optimized rather than treated as separable variables. Experiments show that Na_xTMO_2 with surface coating or structure optimization can maintain the intact particle morphology after long cycling, and at the same time, the

number of cracks is significantly reduced, and the capacity decay rate is significantly reduced. Overall, the above multidimensional strategy, which is centered on three aspects such as composition, structure, and interface, can effectively mitigate the failure process of Na_xTMO_2 due to microcracks, which provides important guidance to enhance the stability of cathodes in SIBs (Fig. 15).

However, in order to further solve the microcracking challenges and push the research results into practical applications in the future, we believe that we need to focus on the following two directions. First, *in situ* and *quasi-in situ* characterization methods need to be further advanced. Deepening the revelation of the whole process of microcracks from germination to expansion means that more advanced *in situ* and quasi-*in situ* characterization techniques need to be developed. At the experimental level, the use of synchrotron X-ray diffraction and neutron diffraction can realize the real-time monitoring of the crystal structure evolution and stress distribution under the battery operating conditions; based on transmission X-ray imaging (*e.g.*, full-field three-dimensional X-ray microtomography STXM, *etc.*), it is expected that the nucleation and expansion path of the cracks inside the particles can be directly observed. Meanwhile, combined with the electrochemical techniques of *in situ* transmission electron microscopy, microscopic details such as localized slip, kink, and crack germination of the layered structure of Na_xTMO_2 during electrochemical processes can be captured in real time at the nanoscale. For processes that cannot be observed continuously, quasi-*in situ* approaches can also complement these observations by providing high-resolution information. Through the fusion of multi-scale and multi-dimensional characterization, researchers can more clearly correlate the causal chain between phase transitions, stress fields and microcracks during electrochemical processes. This will not only help to validate the effectiveness of existing inhibition strategies, but will also reveal crack triggers that have not yet been clarified, providing a basis for new strategy development. Second, there is a need to further advance the validation of applications at the engineering scale. Pushing the microcrack inhibition strategy from the laboratory to the actual battery requires comprehensive validation and optimization at the battery engineering level. On the one hand, the effectiveness of various material modification strategies should be evaluated under conditions close to commercial applications, such as pouch batteries and cylindrical batteries. For example, in thicker electrode films and larger scale cells, the intra-particle stress distribution and crack evolution may show different behaviors from those in laboratory button batteries, which need to be verified through pilot experiments. On the other hand, many factors may affect the formation of microcracks during the industrialized preparation process. Future research needs to focus on optimizing the batch synthesis process of cathode materials to reduce the intrinsic defects and initial stress accumulation during the synthesis process. Also, humidity and residual alkali should be strictly controlled to avoid air erosion during the preparation and storage stages. In addition, at the battery lifetime level, appropriate cell mechanical design and stress buffering strategies should also be introduced, such as optimization of binder and electrolyte formulations, which may also reduce stress accumulation during cycling. The value of microcrack suppression

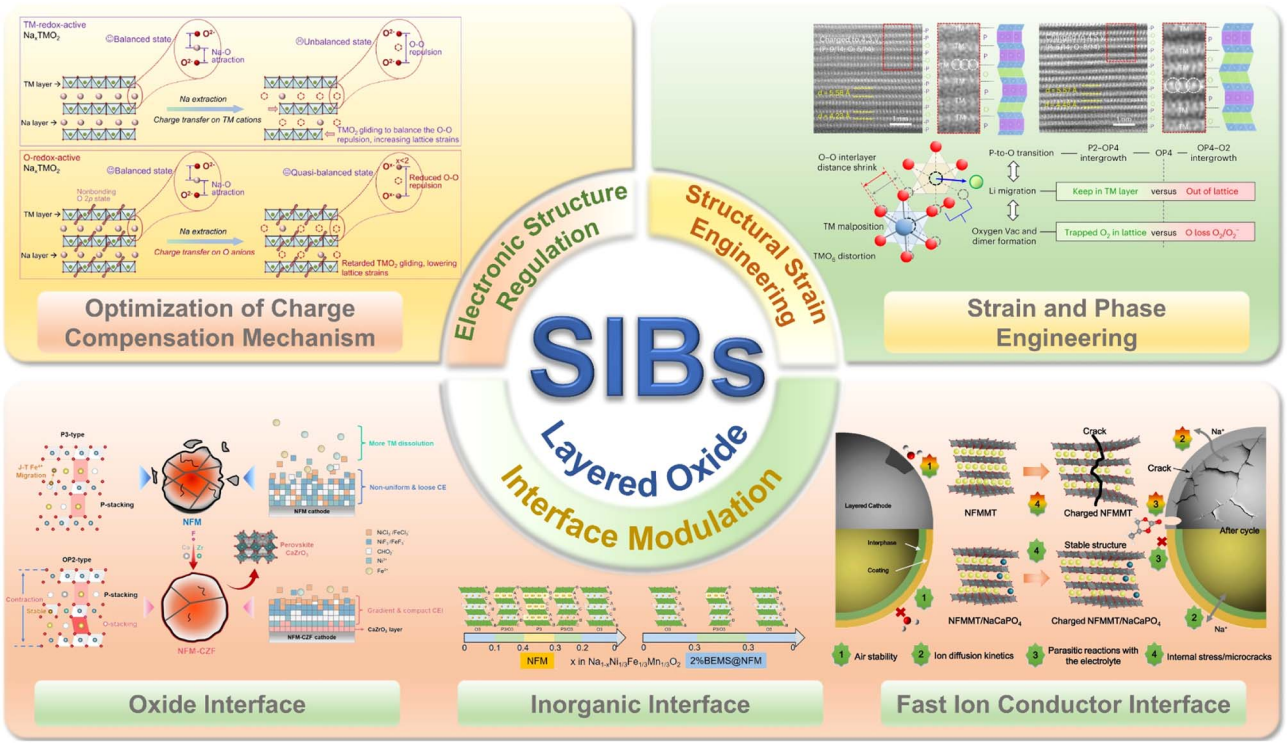

Fig. 15 Schematic summary of microcrack suppression and material design strategies for Na_xTMO_2.

schemes for enhancing the long cycle life and reliability of batteries can only be truly demonstrated through repeated tests under conditions close to practical applications, laying the foundation for their adoption in industrialized SIBs.[162,163]

Author contributions

Ma Qiang: conceptualization, data curation, writing – original draft. Ling-Yi Kong: conceptualization, methodology, data analysis, manuscript revision. Bang-Yuan Guo: software, data curation. Ya-Fang Wang: methodology, data curation. Yan-Fang Zhu: methodology, data curation. Yao Xiao: supervision, funding acquisition.

Conflicts of interest

The authors declare no conflict of interest.

Data availability

No primary research results, software or code have been included and no new data were generated or analysed as part of this review.

Acknowledgements

Qiang Ma and Ling-Yi Kong contributed equally to this work. This work was supported by the National Natural Science Foundation of China (22579131, 52402301, 52472240, and 22509050), National Key R&D Program of China (2024YFA1211900), Key Scientific and Technological Project of Henan Province (252102241004), Wenzhou Key Scientific and Technological Innovation Research Project (ZG2023053), the Open Fund Project of the State Key Laboratory of New Textile Materials and Advanced Processing, Wuhan Textile University, no. FZ2025008, and the Open Fund Project of the State Key Laboratory of Critical Metals Beneficiation, Metallurgy and Purification, Zhengzhou University (CM250205).

References

1 F. Zhang, B. He, Y. Xin, T. Zhu, Y. Zhang, S. Wang, W. Li, Y. Yang and H. Tian, *Chem. Rev.*, 2024, **124**, 4778–4821.
2 J. Wang, Y.-F. Zhu, Y. Su, J.-X. Guo, S. Chen, H.-K. Liu, S.-X. Dou, S.-L. Chou and Y. Xiao, *Chem. Soc. Rev.*, 2024, **53**, 4230–4301.
3 H. Yang, D. Wang, Y. Liu, Y. Liu, B. Zhong, Y. Song, Q. Kong, Z. Wu and X. Guo, *Energy Environ. Sci.*, 2024, **17**, 1756–1780.
4 Z. Li, Y. Wang, J. Wang, C. Wu, W. Wang, Y. Chen, C. Hu, K. Mo, T. Gao, Y.-S. He, Z. Ren, Y. Zhang, X. Liu, N. Liu, L. Chen, K. Wu, C. Shen, Z.-F. Ma and L. Li, *Nat. Commun.*, 2024, **15**, 10216.
5 Y. Zhang, B. Wu, J. Bi, X. Zhang, D. Mu, X. Y. Zhang, L. Zhang, Y. Xiao and F. Wu, *Carbon Energy*, 2024, **6**, e480.
6 M. Zheng, Y. You and J. Lu, *Nat. Rev. Mater.*, 2025, **10**, 355–368.
7 W. Zuo, R. Liu, J. Cai, Y. Hu, M. Almazrouei, X. Liu, T. Cui, X. Jia, E. Apodaca, J. Alami, Z. Chen, T. Li, W. Xu, X. Xiao, D. Parkinson, Y. Yang, G.-L. Xu and K. Amine, *Chem. Rev.*, 2024, **125**, 369–444.
8 S. Zhao, Q. Shi, W. Feng, Y. Liu, X. Yang, X. Zou, X. Lu and Y. Zhao, *Carbon Neutrality*, 2023, **2**, 13.
9 Z. Hong, Z. C. Jian, Y. F. Zhu, Y. J. Li, Q. C. Ling, H. Xin, D. Wang, C. Wu and Y. Xiao, *Chem. Sci.*, 2025, **16**, 17058–17085.
10 Y.-J. Guo, R.-X. Jin, M. Fan, W.-P. Wang, S. Xin, L.-J. Wan and Y.-G. Guo, *Chem. Soc. Rev.*, 2024, **53**, 7828–7874.
11 Z. Chen, Y. Deng, J. Kong, W. Fu, C. Liu, T. Jin and L. Jiao, *Adv. Mater.*, 2024, **36**, 2402008.
12 Z.-C. Jian, Y.-F. Liu, Y.-F. Zhu, J.-Y. Li, H.-Y. Hu, J. Wang, L.-Y. Kong, X.-B. Jia, H.-X. Liu, J.-X. Guo, M.-Y. Li, Y.-S. Xu, J.-F. Mao, S.-L. Zhang, Y. Su, S.-X. Dou, S.-L. Chou and Y. Xiao, *Nano Energy*, 2024, **125**, 109528.
13 P. Li, T. Yuan, J. Qiu, H. Che, Q. Ma, Y. Pang, Z.-F. Ma and S. Zheng, *Mater. Sci. Eng. R Rep.*, 2025, **163**, 100902.
14 C. Che, F. Wu, Y. Li, Y. Li, S. Li, C. Wu and Y. Bai, *Adv. Mater.*, 2024, **36**, 2402291.
15 Z. C. Jian, J. X. Guo, Y. F. Liu, Y. F. Zhu, J. Wang and Y. Xiao, *Chem. Sci.*, 2024, **15**, 19698–19728.
16 I. Moeez, A. H. U. Bhatti, M. K. Cho, D. Susanto, M. Akbar, G. Ali and K. Y. Chung, *Carbon Energy*, 2025, **7**, e658.
17 B. Peng, G. Wan, N. Ahmad, L. Yu, X. Ma and G. Zhang, *Adv. Energy Mater.*, 2023, **13**, 2300334.
18 J.-Y. Li, H.-Y. Hu, H.-W. Li, Y.-F. Liu, Y. Su, X.-B. Jia, L.-F. Zhao, Y.-M. Fan, Q.-F. Gu, H. Zhang, W. K. Pang, Y.-F. Zhu, J.-Z. Wang, S.-X. Dou, S.-L. Chou and Y. Xiao, *ACS Nano*, 2024, **18**, 12945–12956.
19 T. Zhang, Y. Li, Z. Song, Y. Huang, F. Li, S. Cheng and F. Li, *J. Energy Chem.*, 2025, **103**, 294–315.
20 Z. Yu, C. Gan, A. S. Mijailovic, A. Stone, R. Hurt, C. L. Pernia, X. Xiao, C. Shi and B. W. Sheldon, *Adv. Energy Mater.*, 2024, **15**, 2403179.
21 Y. Kuang, Y. Wu, H. Zhang and H. Sun, *Molecules*, 2024, **29**, 5988.
22 Y. Li, G. Liu, J. Che, L. Chen, X. Wang, G. Wang, L. Lei, J. Hou, S. Li, J. Wang, Y. Xu and Y. Zhao, *Interdiscip. Mater.*, 2024, **4**, 24–51.
23 L.-Y. Kong, H.-X. Liu, Y.-F. Zhu, J.-Y. Li, Y. Su, H.-W. Li, H.-Y. Hu, Y.-F. Liu, M.-J. Yang, Z.-C. Jian, X.-B. Jia, S.-L. Chou and Y. Xiao, *Sci. China Chem.*, 2023, **67**, 191–213.
24 Q. Pang, M. Zhang, Y. Song, Y. Liu, M. Tang, S. Su, L. Qiu, Y. Xiao and X. Guo, *Chem. Sci.*, 2025, **16**, 4237–4244.
25 B. Wang, X. Chen, X. Chen, Y. Wang, D. Qi, Y. Huang, X. Jiang, J.-H. Liu, P. Yan and Y. Xiao, *eScience Energy*, 2025, **1**, 100008.
26 L. F. Pfeiffer, Y. Li, M. Mundszinger, J. Geisler, C. Pfeifer, D. Mikhailova, A. Omar, V. Baran, J. Biskupek, U. Kaiser, P. Adelhelm, M. Wohlfahrt-Mehrens, S. Passerini and P. Axmann, *Chem. Mater.*, 2023, **35**, 8065–8080.
27 C. Wang, X. Wang, P. Zou, R. Zhang, S. Wang, B. Song, K.-B. Low and H. L. Xin, *Matter*, 2023, **6**, 1265–1277.
28 H.-Y. Hu, Y.-C. Li, Y.-F. Zhu, H. Liu, W. Xiang, J.-Z. Wang and Y. Xiao, *Chem. Sci.*, 2025, **16**, 15714–15722.

29 Y. Zhang, S. Hao, F. Pei, X. Xiao, C. Lu, X. Lin, Z. Li, H. Ji, Y. Shen, L. Yuan, Z. Li and Y. Huang, *Natl. Sci. Rev.*, 2024, **11**, 254.
30 W. Liang, Y. Zhao, L. Shi, Z. Wang, Y. Wang, M. Zhang and S. Yuan, *Particuology*, 2024, **86**, 67–85.
31 B. Wu, R. Yi, Y. Xu, P. Gao, Y. Bi, L. Novák, Z. Liu, E. Hu, N. Wang, J. Rijssenbeek, S. Venkatachalam, J. Wu, D. Liu, X. Cao and J. Xiao, *Nat. Energy*, 2025, **10**, 605–615.
32 W. Zuo, J. Gim, T. Li, D. Hou, Y. Gao, S. Zhou, C. Zhao, X. Jia, Z. Yang, Y. Liu, W. Xu, X. Xiao, G.-L. Xu and K. Amine, *Nat. Nanotechnol.*, 2024, **19**, 1644–1653.
33 G. L. Xu, X. Liu, X. Zhou, C. Zhao, I. Hwang, A. Daali, Z. Yang, Y. Ren, C. J. Sun, Z. Chen, Y. Liu and K. Amine, *Nat. Commun.*, 2022, **13**, 436.
34 Y. F. Liu, K. Han, D. N. Peng, L. Y. Kong, Y. Su, H. W. Li, H. Y. Hu, J. Y. Li, H. R. Wang, Z. Q. Fu, Q. Ma, Y. F. Zhu, R. R. Tang, S. L. Chou, Y. Xiao and X. W. Wu, *InfoMat*, 2023, **5**, e12422.
35 Q. Zhao, R. Wang, M. Gao, F. K. Butt, J. Jia, H. Wu and Y. Zhu, *Nano Res.*, 2023, **17**, 1441–1464.
36 Y.-F. Liu, H.-Y. Hu, J.-Y. Li, H. Wang, Y. Zhao, J. Wang, Y.-B. Wu, Y.-J. Li, G.-Y. Zhang, Q.-Q. Sun, Y.-F. Zhu, R.-R. Tang, X.-W. Wu, J.-Z. Wang, S.-X. Dou, S.-L. Chou and Y. Xiao, *Sci. China Chem.*, 2024, **67**, 4242–4250.
37 H. Zheng, M. Fan, C. Zhang, W. He, G. Gao, Y. Liu, L. Wang, Q. Xie, D. L. Peng and J. Lu, *Adv. Mater.*, 2024, **37**, 2414443.
38 A. Gao, S. Shen, T. Shang, Y. Shi, H. Zhang, W. Lin, S. Wang, T. Lin, P. Ji, Y. Wang, Y. Chen, B. Yu, X. Lu, W. Zhong, Q. Zhang and L. Gu, *Sci. Adv.*, 2025, **10**, 4906.
39 X. M. Shi, K. Kawai, M. Okubo and A. Yamada, *Adv. Energy Mater.*, 2025, **15**, 2405714.
40 Y. Xiao, Q. Q. Sun, D. Chen, J. Wang, J. Ding, P. Tan, Y. Sun, S. Zhang, P. F. Wang, J. Mao and Y. F. Zhu, *Adv. Mater.*, 2025, **37**, 2504312.
41 X. M. Shi, K. Kawai, M. Okubo and A. Yamada, *Adv. Energy Mater.*, 2025, **15**, 2405714.
42 X. Li, A. Gao, Q. Zhang, H. Yu, P. Ji, D. Xiao, X. Wang, D. Su, X. Rong, X. Yu, H. Li, Y. S. Hu and L. Gu, *Carbon Energy*, 2023, **6**, e389.
43 W. Huang, T. Liu, L. Yu, J. Wang, T. Zhou, J. Liu, T. Li, R. Amine, X. Xiao, M. Ge, L. Ma, S. N. Ehrlich, M. V. Holt, J. Wen and K. Amine, *Science*, 2024, **384**, 912–919.
44 S. Xu, L. Zhao, S. Li and S. Guo, *Chem. Commun.*, 2025, **61**, 4147–4159.
45 R. Yu, W. Zeng, L. Zhou, G. Van Tendeloo, L. Mai, Z. Yao and J. Wu, *Cell Rep. Phys. Sci.*, 2023, **4**, 101480.
46 Y. J. Li, Y. F. Zhu, B. B. Chen, X. B. Jia, H. Xin, G. Z. Zhao, G. Zhu, S. X. Dou and Y. Xiao, *Adv. Funct. Mater.*, 2025, **35**, 2504096.
47 G. W. Nam, N.-Y. Park, K.-J. Park, J. Yang, J. Liu, C. S. Yoon and Y.-K. Sun, *ACS Energy Lett.*, 2019, **4**, 2995–3001.
48 D. Eum, S.-O. Park, H.-Y. Jang, Y. Jeon, J.-H. Song, S. Han, K. Kim and K. Kang, *Nat. Mater.*, 2024, **23**, 1093–1099.
49 Y. Huang, W. Zeng, K. Li and X. Zhu, *Microstructures*, 2024, **4**, 2024027.
50 J. W. Somerville, A. Sobkowiak, N. Tapia-Ruiz, J. Billaud, J. G. Lozano, R. A. House, L. C. Gallington, T. Ericsson, L. Häggström, M. R. Roberts, U. Maitra and P. G. Bruce, *Energy Environ. Sci.*, 2019, **12**, 2223–2232.
51 K. Wang, P. Yan and M. Sui, *Nano Energy*, 2018, **54**, 148–155.
52 T. Y. Yu, H. H. Ryu, G. Han and Y. K. Sun, *Adv. Energy Mater.*, 2020, **10**, 2001609.
53 Y. Li, X. Li, C. Du, H. Sun, Y. Zhang, Q. Liu, T. Yang, J. Zhao, C. Delmas, S. J. Harris, H. Chen, Q. Huang, Y. Tang, L. Zhang, T. Zhu and J. Huang, *ACS Energy Lett.*, 2021, **6**, 3960–3969.
54 T. Sun, B. Wu, S. Deng, Y.-J. Guo, J.-L. Shi, X. Zhang, X. Shi, G. Qian, J. Wang, P. Pianetta, J. Zhou, Y.-G. Guo and Y. Liu, *J. Am. Chem. Soc.*, 2025, **147**, 21375–21384.
55 X. L. Li, T. Wang, Y. Yuan, X. Y. Yue, Q. C. Wang, J. Y. Wang, J. Zhong, R. Q. Lin, Y. Yao, X. J. Wu, X. Q. Yu, Z. W. Fu, Y. Y. Xia, X. Q. Yang, T. Liu, K. Amine, Z. Shadike, Y. N. Zhou and J. Lu, *Adv. Mater.*, 2021, **33**, e2008194.
56 X. Rong, E. Hu, Y. Lu, F. Meng, C. Zhao, X. Wang, Q. Zhang, X. Yu, L. Gu, Y.-S. Hu, H. Li, X. Huang, X.-Q. Yang, C. Delmas and L. Chen, *Joule*, 2019, **3**, 503–517.
57 Y. Bi, J. Tao, Y. Wu, L. Li, Y. Xu, E. Hu, B. Wu, J. Hu, C. Wang, J.-G. Zhang, Y. Qi and J. Xiao, *Science*, 2020, **370**, 1313–1317.
58 X.-H. Meng, T. Lin, H. Mao, J.-L. Shi, H. Sheng, Y.-G. Zou, M. Fan, K. Jiang, R.-J. Xiao, D. Xiao, L. Gu, L.-J. Wan and Y.-G. Guo, *J. Am. Chem. Soc.*, 2022, **144**, 11338–11347.
59 J. Huang, Z. Xue, S.-J. Lee, H. Chen, X. Ji and K. Du, *J. Am. Chem. Soc.*, 2025, **147**, 22444–22452.
60 T. Yang, X. Wang, Z. Liu and Q. Liu, *ACS Nano*, 2024, **18**, 18834–18851.
61 J. S. Garcia, G. D. D. Sanglay, L. M. E. Sapanta, M. S. Palaganas, L. A. Limjuco and J. D. Ocon, *Mater. Today Energy*, 2025, **53**, 101969.
62 H. Li, J. Wang, S. Xu, A. Chen, H. Lu, Y. Jin, S. Guo and J. Zhu, *Adv. Mater.*, 2024, **36**, 2403073.
63 S. Jia, S. Kumakura and E. McCalla, *Energy Environ. Sci.*, 2024, **17**, 4343–4389.
64 Y. You, A. Dolocan, W. Li and A. Manthiram, *Nano Lett.*, 2018, **19**, 182–188.
65 Y. Yang, Z. Wang, C. Du, B. Wang, X. Li, S. Wu, X. Li, X. Zhang, X. Wang, Y. Niu, F. Ding, X. Rong, Y. Lu, N. Zhang, J. Xu, R. Xiao, Q. Zhang, X. Wang, W. Yin, J. Zhao, L. Chen, J. Huang and Y.-S. Hu, *Science*, 2024, **385**, 744–752.
66 Y. Huang, W. Zhang, Y. Zhou, Y. Wang, L. Li, H. Shao, X. Li, Z. Hong, H. Xia, Y. Shen and L. Chen, *ACS Nano*, 2024, **18**, 13106–13116.
67 H. Liu, L. Kong, H. Wang, J. Li, J. Wang, Y. Zhu, H. Li, Z. Jian, X. Jia, Y. Su, S. Zhang, J. Mao, S. Chen, Y. Liu, S. Chou and Y. Xiao, *Adv. Mater.*, 2024, **36**, 2407994.
68 A. Zeng, N. Li, H. Zhang, S. Qiu, Z. Xu, Y. Zhang, W. Yin, E. Zhao and X. Xiao, *Angew. Chem., Int. Ed.*, 2025, **64**, e202514220.
69 S. Lee, L. Su, A. Mesnier, Z. Cui and A. Manthiram, *Joule*, 2023, **7**, 2430–2444.
70 W. Ou, S. D. Marks, R. F. de Menezes, R. He, Z. Zhang, C. Sindt, J. Thurston, C. Jaye, B. Cowie, L. Thomsen, Z. Zhuo, J. Guo, W. Yang, Z. Dong, R. Tenent,

K. G. Sprenger and M. F. Toney, *Adv. Energy Mater.*, 2025, **15**, 2404652.
71 J. Lin, H. Peng, P. Huang, T. Naren, C. Liang, G. Kuang, L. Chen, C. Zhang and W. Wei, *Adv. Funct. Mater.*, 2023, **33**, 2307061.
72 G. Åvall and P. Adelhelm, *Nat. Energy*, 2022, **7**, 682–683.
73 X. Zhang, Z. Wang, X. Li, Y. Su, Z. Ye, L. Zhang, Q. Huang, Y. Tang and J. Huang, *Mater. Horiz.*, 2023, **10**, 1856–1864.
74 Q. Li, Y. Li, M. Liu, Y. Li, H. Zhao, H. Ren, Y. Zhao, Q. Zhou, X. Feng, J. Shi, C. Wu and Y. Bai, *Adv. Mater.*, 2025, **37**, 2415610.
75 S.-Q. Su, Q.-C. Ling, Y.-J. Li, Y.-P. Yan, Y.-F. Zhu and Y. Xiao, *Chem. Sci.*, 2025, **16**, 22852–22869.
76 Z. Lun, A. J. Merryweather, A. Mahadevegowda, S. S. Pandurangi, C. Xu, S. Fairclough, V. S. Deshpande, N. A. Fleck, C. Ducati, C. Schnedermann, A. Rao and C. P. Grey, *Energy Environ. Sci.*, 2025, **18**, 4097–4107.
77 S. Wang, S. Chen, X. Liu, G. Feng, B. Zhang, W. Xing, Y. Xiao, H. Liu and W. Xiang, *Chem. Sci.*, 2026, **17**, 3212–3223.
78 H. Y. Hu, M. Yang, D. Chen, N. H. Xu, J. Y. Li, Y. F. Zhu, Y. B. Wu, H. H. Dong, J. Wang, C. Yao, Y. Yan, S. Chen, N. Wang, W. K. Pang, Y. Sun, J. Z. Wang and Y. Xiao, *Angew. Chem., Int. Ed.*, 2025, **65**, e19108.
79 Y. Song, B. Wang, Y. Cui, P. Liu, X. Gao, X. Li, L. Zhu, Q. Xue, Y. Tang and W. Xing, *eScience*, 2025, **6**, 100435.
80 X. Yang, L. Wang, M. Zhao, L. Peng, Y. Wu, B. Zhu, L. Chen and J. Li, *Chem. Sci.*, 2025, **16**, 17703–17713.
81 Y. Song, W. Dong, Z. Lv, B. Han, J. Li, X. Wang, X. Wang, J. Chen, C. Dong, Z. Mao and L. Zhang, *Carbon Energy*, 2025, **8**, e70142.
82 Q. Wang, G. Yu, B. Luo, W. Ji, Z. Liu, M. Li, Y. Nong, Y. Tian, X. Wang, J. Zhang, C.-L. Chen, C.-K. Chang, Z. Sang, Z. Zhao, R. Zhao and J. Liang, *ACS Nano*, 2024, **18**, 18622–18634.
83 Z. Liu, R. Liu, S. Xu, J. Tian, J. Li, H. Li, T. Yu, S. Chu, A. M. D'Angelo, W. K. Pang, L. Zhang, S. Guo and H. Zhou, *Angew. Chem., Int. Ed.*, 2024, **63**, e202405620.
84 C. Zhao, Z. Yao, Q. Wang, H. Li, J. Wang, M. Liu, S. Ganapathy, Y. Lu, J. Cabana, B. Li, X. Bai, A. Aspuru-Guzik, M. Wagemaker, L. Chen and Y.-S. Hu, *J. Am. Chem. Soc.*, 2020, **142**, 5742–5750.
85 Y. Tang, Q. Zhang, W. Zuo, S. Zhou, G. Zeng, B. Zhang, H. Zhang, Z. Huang, L. Zheng, J. Xu, W. Yin, Y. Qiu, Y. Xiao, Q. Zhang, T. Zhao, H.-G. Liao, I. Hwang, C.-J. Sun, K. Amine, Q. Wang, Y. Sun, G.-L. Xu, L. Gu, Y. Qiao and S.-G. Sun, *Nat Sustainability*, 2024, **7**, 348–359.
86 X. Xu, Y. Chu, Y. Mu, X. Wei, Q. Zhang, H. Rao, H. Gu, L. Pan, M. Han, Y. Wang, L. Zeng and L. Wei, *ACS Nano*, 2025, **19**, 31395–31406.
87 K. Wang, H. Wan, P. Yan, X. Chen, J. Fu, Z. Liu, H. Deng, F. Gao and M. Sui, *Adv. Mater.*, 2019, **31**, e1904816.
88 C. Cai, X. Li, J. Li, R. Yu, P. Hu, T. Zhu, T. Li, S. Lee, N. Xu, H. Fan, J. Wu, L. Zhou, L. Mai and K. Amine, *Nat. Commun.*, 2025, **16**, 100.
89 F. Ding, C. Zhao, D. Xiao, X. Rong, H. Wang, Y. Li, Y. Yang, Y. Lu and Y.-S. Hu, *J. Am. Chem. Soc.*, 2022, **144**, 8286–8295.
90 X.-B. Jia, Q.-Q. Peng, Y.-F. Liu, D.-C. Chen, J. Wang, J.-Y. Li, Y.-F. Zhu, N.-H. Xu, L.-Y. Kong, H.-X. Liu, G.-Y. Zhang, Z.-C. Jian, C. Cheng, H.-H. Dong, L. Zhang, Y. Sun, S.-Q. Chen, X.-D. Guo, S. Dou and Y. Xiao, *Nat. Commun.*, 2025, **16**, 10477.
91 B. Wang, K. Li, G. Xu, Z. Zhang, X. Wang, J. Sun, Y. Song, X. Zhang, Y. Liang, D. Kong, Y. Qiu, Q. Teng, X. Cui, J. Chen, J. Zhao, J. Wang, H. Yang, J. Huang and Y. Tang, *Angew. Chem., Int. Ed.*, 2025, **64**, e202502725.
92 S. Jiao, Y. Li, T. Lin, S. Feng, C. Zhang, H. Pan, W. Lin, X. Yu, L. Gu, X. Huang, L. Chen and H. Li, *J. Am. Chem. Soc.*, 2025, **147**, 22839–22850.
93 Y. Huang, S. Gu, X. Xu, Z. An, X. Han, Y. Cao, D. He, F. Zhang, H. Guo, Y. Liu, X. Liao, G. Liu, P. Liu, F. Wu, Y. Li, Z. Wang, Z. Wang, C. Ding, Y. Wang, J. Chen, M. Yang, F. Jiang, Y. Deng, Z. Xu and Z. Lu, *Adv. Mater.*, 2025, **37**, 2408012.
94 N. Li, W. Yin, B. Wang, F. Wang, X. Xiao, J. Zhao and E. Zhao, *Energy Environ. Mater.*, 2023, **7**, e12671.
95 N. Li, E. Zhao, Z. Zhang, W. Yin, L. He, B. Wang, F. Wang, X. Xiao and J. Zhao, *Adv. Mater.*, 2024, **36**, 2408984.
96 L. Sun, Z. Wu, M. Hou, Y. Ni, H. Sun, P. Jiao, H. Li, W. Zhang, L. Zhang, K. Zhang, F. Cheng and J. Chen, *Energy Environ. Sci.*, 2024, **17**, 210–218.
97 S. Gao, Z. Zhu, H. Fang, K. Feng, J. Zhong, M. Hou, Y. Guo, F. Li, W. Zhang, Z. Ma and F. Li, *Adv. Mater.*, 2024, **36**, 2311523.
98 Y. Liu, Y. Xin, B. He, F. Zhang, C. Wang and H. Tian, *Adv. Mater.*, 2025, **37**, 2417353.
99 Y. Yang, J. Cai, Y. Zuo, K. Zhang, C. Gao, L. Zhou, Z. Chen, W. Chu and D. Xia, *Energy Storage Mater.*, 2024, **71**, 103587.
100 J. Wang, D. Chen, H. Dong, Q.-Q. Sun, M.-Y. Li, G.-Y. Zhang, H.-Y. Hu, Y. Pian, J. Yu, Y.-F. Zhu, H. Wei, Y. Sun, S. Zhao, H. Chu, J. Liu and Y. Xiao, *ACS Nano*, 2025, **19**, 31901–31914.
101 X. B. Jia, J. Wang, Y. F. Liu, Y. F. Zhu, J. Y. Li, Y. J. Li, S. L. Chou and Y. Xiao, *Adv. Mater.*, 2024, **36**, 2307938.
102 Y. B. Wu, H. Y. Hu, J. Y. Li, H. H. Dong, Y. F. Zhu, S. Q. Chen, N. N. Wang, J. Z. Wang and Y. Xiao, *Chem. Sci.*, 2025, **16**, 3928–3937.
103 C. Jiang, Y. Wang, Y. Xin, X. Ding, S. Liu, Y. Pang, B. Chen, Y. Wang, L. Liu, F. Wu and H. Gao, *Carbon Neutralization*, 2024, **3**, 233–244.
104 W. Zuo, X. Liu, J. Qiu, D. Zhang, Z. Xiao, J. Xie, F. Ren, J. Wang, Y. Li, G. F. Ortiz, W. Wen, S. Wu, M.-S. Wang, R. Fu and Y. Yang, *Nat. Commun.*, 2021, **12**, 4903.
105 K. Zhang, Z. Xu, G. Li, R. J. Luo, C. Ma, Y. Wang, Y. N. Zhou and Y. Xia, *Adv. Energy Mater.*, 2023, **13**, 2302793.
106 Y. Mao, H. Gong, X. Wang, Y. Cao, S. Wang, K. Ma, X. G. Fuku, C. Zhou and J. Sun, *Adv. Energy Mater.*, 2025, **15**, 2502592.
107 T. Zhang, M. Ren, Y. Huang, F. Li, W. Hua, S. Indris and F. Li, *Angew. Chem., Int. Ed.*, 2024, **63**, e202316949.
108 J. Kuang, Z. Liu, L. Fu, S. You, M. Zhang, Y. Wang, N. Ding, D. Sun, Y. Tang and H. Wang, *Angew. Chem., Int. Ed.*, 2025, **64**, e202500715.

109 B. Peng, X. Huang, C. Xu, Z. Huang, R. Zhu, C. Jin, L. Wang and H. Zhou, *Adv. Mater.*, 2025, **38**, e14943.
110 T. Liu, L. Yu, J. Lu, T. Zhou, X. Huang, Z. Cai, A. Dai, J. Gim, Y. Ren, X. Xiao, M. V. Holt, Y. S. Chu, I. Arslan, J. Wen and K. Amine, *Nat. Commun.*, 2021, **12**, 6024.
111 Z. Zhang, W. Yin, J. Peng, F. Zheng, Q. Pan, H. Wang, Q. Li and S. Hu, *Chem. Sci.*, 2026, **17**, 3819–3827.
112 M. Li, H. Zhuo, J. Lei, Y. Guo, Y. Yuan, K. Wang, Z. Liao, W. Xia, D. Geng, X. Sun, J. Hu and B. Xiao, *Nat. Commun.*, 2025, **16**, 2010.
113 H.-Y. Hu, J.-Y. Li, Y.-F. Liu, Y.-F. Zhu, H.-W. Li, X.-B. Jia, Z.-C. Jian, H.-X. Liu, L.-Y. Kong, Z.-Q. Li, H.-H. Dong, M.-K. Zhang, L. Qiu, J.-Q. Wang, S.-Q. Chen, X.-W. Wu, X.-D. Guo and Y. Xiao, *Chem. Sci.*, 2024, **15**, 5192–5200.
114 F. Ding, P. Ji, Z. Han, X. Hou, Y. Yang, Z. Hu, Y. Niu, Y. Liu, J. Zhang, X. Rong, Y. Lu, H. Mao, D. Su, L. Chen and Y.-S. Hu, *Nat. Energy*, 2024, **9**, 1529–1539.
115 H. Wang, Y. Mei, J. Gao, L. Ni, N. Hong, L. Ma, G. Kwon, J. Huang, Y. He, W. Deng, G. Zou, H. Hou, C. Liang, T. Liu, X. Ji and K. Amine, *J. Am. Chem. Soc.*, 2025, **147**, 4810–4820.
116 H. Wang, T. Liu, H. Chen, Y. Mei, J. Gao, L. Ni, N. Hong, J. Huang, X. Hu, W. Deng, G. Zou, H. Hou, D. S. Silvester, C. E. Banks, X. Ji and K. Amine, *Nat. Commun.*, 2025, **16**, 4409.
117 Q. Huang, D. Cheng, B. Wu, Z. Liu, K. Zhang, Y. Zou, L. Li and Y. Chen, *Adv. Funct. Mater.*, 2025, **36**, e18419.
118 L. Y. Kong, Z. Q. Li, H. X. Liu, X. Y. Li, Y. F. Zhu, J. Y. Li, P. Tan, M. Yang, J. F. Mao, W. K. Pang and Y. Xiao, *Angew. Chem., Int. Ed.*, 2025, **64**, e202517300.
119 X. Wang, Q. Zhang, C. Zhao, H. Li, B. Zhang, G. Zeng, Y. Tang, Z. Huang, I. Hwang, H. Zhang, S. Zhou, Y. Qiu, Y. Xiao, J. Cabana, C.-J. Sun, K. Amine, Y. Sun, Q. Wang, G.-L. Xu, L. Gu, Y. Qiao and S.-G. Sun, *Nat. Energy*, 2024, **9**, 184–196.
120 N. Jiang, J. Yu, Z. Wu, J. Zhao, Y. Zeng, H. Li, M. Meng, Y. He, P. Jiao, H. Pan, H. Wang, J. Qi, Z. Hu, K. Zhang and J. Chen, *Angew. Chem., Int. Ed.*, 2024, **63**, e202410080.
121 R. Zhang, C. Wang, P. Zou, R. Lin, L. Ma, L. Yin, T. Li, W. Xu, H. Jia, Q. Li, S. Sainio, K. Kisslinger, S. E. Trask, S. N. Ehrlich, Y. Yang, A. M. Kiss, M. Ge, B. J. Polzin, S. J. Lee, W. Xu, Y. Ren and H. L. Xin, *Nature*, 2022, **610**, 67–73.
122 R. Liu, W. Huang, J. Liu, Y. Li, J. Wang, Q. Liu, L. Ma, G. Kwon, S. N. Ehrlich, Y. Wu, T. Liu, K. Amine and H. Li, *Adv. Mater.*, 2024, **36**, 2401048.
123 W. Zuo, J. Qiu, X. Liu, B. Zheng, Y. Zhao, J. Li, H. He, K. Zhou, Z. Xiao, Q. Li, G. F. Ortiz and Y. Yang, *Energy Storage Mater.*, 2020, **26**, 503–512.
124 N. Hong, S. Zhang, J. Li, H. Wang, J. Huang, X. Hu, B. Zhang, F. Hua, J. Zeng, W. Jian, C. Sun, N. Bugday, W. Deng, G. Zou, H. Hou, Z. Hu, Z. Long, Y. Wu and X. Ji, *Angew. Chem., Int. Ed.*, 2025, **64**, e202423479.
125 X. Liang, T.-Y. Yu, H.-H. Ryu and Y.-K. Sun, *Energy Storage Mater.*, 2022, **47**, 515–525.
126 Z.-C. Jian, W. Shi, Y. Liu, X. Li, J. Li, Y.-F. Zhu, X. Zhu, Y. Li, P. Tan, P.-F. Wang, S. Chen, S. Zhang, J. Mao, G. Zhou, X. Guo, J. Wang, S.-X. Dou and Y. Xiao, *Energy Environ. Sci.*, 2025, **18**, 7995–8008.
127 B. Zheng, H. Qian, G. Cheng, C. Yuan, Y. Cheng, M.-S. Wang, X. Liu and Y. Xiang, *Energy Storage Mater.*, 2025, **74**, 103868.
128 D. Yang, Y. Long, X. W. Gao, Z. Zhao, H. Chen, Q. Lai, C. Li, R. Niu, Z. Liu, Q. Gu and W. B. Luo, *Adv. Energy Mater.*, 2024, **15**, 2404999.
129 D. R. Yang, L. Chen, X. W. Gao, Z. Zhao, Q. S. Lai, H. Chen, Y. Long, Q. Gu, Z. M. Liu and W. B. Luo, *ACS Nano*, 2025, **19**, 2834–2847.
130 C. Xie, J. Zhou, C. Chen, Y. Li, S. Kumakura, V. Ganesan, H. Huang and Y. Yang, *Adv. Energy Mater.*, 2025, DOI: 10.1002/aenm.202504771.
131 Q. Zhang, J. Wang, Y. Chu, W. Huang, X. Huang, X. Xiao, L. Ma, T. Liu, K. Amine, J. Lu and C. Yang, *Nat. Energy*, 2025, **10**, 1001–1012.
132 M. Ahangari, M. Zhou and H. Luo, *Micromachines*, 2025, **16**, 137.
133 L. Wang, T. Liu, T. Wu and J. Lu, *Nature*, 2022, **611**, 61–67.
134 S. Li, F. Liu, S. Zhang, X. Gao, W. Zhou, Y. Xie, Y. Lai and Z. Zhang, *Angew. Chem., Int. Ed.*, 2025, **64**, e202424079.
135 H. Bi, X. Sun, B. Zhao, R. Li, Y. Zhang, X. Wang, M. Zhang, D. Luo and Z. Chen, *Adv. Funct. Mater.*, 2025, **35**, e07781.
136 Y. Yu, W. Kong, Q. Li, D. Ning, G. Schuck, G. Schumacher, C. Su and X. Liu, *ACS Appl. Energy Mater.*, 2020, **3**, 933–942.
137 K. Xu, M. Yan, Y.-X. Chang, X. Xing, L. Yu and S. Xu, *Electrochim. Acta*, 2022, **419**, 140394.
138 Z. Xu, X. Guo, X. Zeng, J. Liu, J. Yin, M. Ren, J. Wang, T. Qin, Z. Zhang, L. Li, K. Amine, Y. Yuan and T. Liu, *J. Am. Chem. Soc.*, 2025, **147**, 3967–3980.
139 M. Chang, F. Cheng, W. Zhang, M. Liao, Q. Li, C. Fang and J. Han, *ACS Nano*, 2024, **19**, 712–721.
140 T. Yuan, P. Li, Y. Sun, H. Che, Q. Zheng, Y. Zhang, S. Huang, J. Qiu, Y. Pang, J. Yang, Z. F. Ma and S. Zheng, *Adv. Funct. Mater.*, 2024, **35**, 2414627.
141 W. Xu, R. Dang, L. Zhou, Y. Yang, T. Lin, Q. Guo, F. Xie, Z. Hu, F. Ding, Y. Liu, Y. Liu, H. Mao, J. Hong, Z. Zuo, X. Wang, R. Yang, X. Jin, X. Hou, Y. Lu, X. Rong, N. Xu and Y. S. Hu, *Adv. Mater.*, 2023, **35**, 2301314.
142 X. Liang, X. Song, H. H. Sun, H. Kim, M.-C. Kim and Y.-K. Sun, *Nat. Commun.*, 2025, **16**, 3505.
143 H. Wang, F. Ding, Y. Wang, Z. Han, R. Dang, H. Yu, Y. Yang, Z. Chen, Y. Li, F. Xie, S. Zhang, H. Zhang, D. Song, X. Rong, L. Zhang, J. Xu, W. Yin, Y. Lu, R. Xiao, D. Su, L. Chen and Y.-S. Hu, *ACS Energy Lett.*, 2023, **8**, 1434–1444.
144 X.-Y. Zhang, L.-Y. Kong, J. Ding, Y.-F. Zhu, J.-Y. Li, Z.-C. Jian, H. Xin, M.-Y. Li, P. Tan, W. K. Pang, S.-X. Dou and Y. Xiao, *ACS Energy Lett.*, 2025, **10**, 2858–2867.
145 L.-Y. Kong, J.-Y. Li, H.-X. Liu, Y.-F. Zhu, J. Wang, Y. Liu, X.-Y. Zhang, H.-Y. Hu, H. Dong, Z.-C. Jian, C. Cheng, S. Chen, L. Zhang, J.-Z. Wang, S. Chou and Y. Xiao, *J. Am. Chem. Soc.*, 2024, **146**, 32317–32332.
146 X. Liu, J. Hao, M. Zhang, B. Zheng, D. Zhao, Y. Cheng, Z. He, M. Su, C. Xie, M. Luo, P. Shan, M. Tao, Z. Liang, Y. Xiang and Y. Yang, *ACS Appl. Mater. Interfaces*, 2022, **14**, 30398–30409.

147 C. Chen, Z. Han, S. Chen, S. Qi, X. Lan, C. Zhang, L. Chen, P. Wang and W. Wei, *ACS Appl. Mater. Interfaces*, 2020, **12**, 7144–7152.
148 X. Yang, Y. Li, X. Li, T. Lin, W. Lin, P. Li, D. Xiao, S. Wang and H. Pan, *ACS Energy Lett.*, 2025, **10**, 1491–1498.
149 K. Tang, Y. Huang, X. Xie, S. Cao, L. Liu, M. Liu, Y. Huang, B. Chang, Z. Luo and X. Wang, *Chem. Eng. J.*, 2020, **384**, 123234.
150 Q. Deng, F. Zheng, W. Zhong, Q. Pan, Y. Liu, Y. Li, Y. Li, J. Hu, C. Yang and M. Liu, *Chem. Eng. J.*, 2021, **404**, 126446.
151 Z. Li, P. Huang, J. Zhang, Z. Guo, Z. Liu, L. Chen, J. Zhang, J. Luo, X. Tao, Z. Miao, H. Jiang, C. Wang, X. Ye, X. Wu, W.-D. Liu, R. Liu, Y. Chen and W. Hu, *Energy Environ. Sci.*, 2025, **18**, 2962–2972.
152 C.-H. Jo, J.-H. Jo, H. Yashiro, S.-J. Kim, Y.-K. Sun and S.-T. Myung, *Adv. Energy Mater.*, 2018, **8**, 1702942.
153 X. Yang, Y. Li, X. Li, T. Lin, W. Lin, P. Li, D. Xiao, S. Wang and H. Pan, *Energy Storage Mater.*, 2025, **76**, 104158.
154 H. H. Sun, J. Y. Hwang, C. S. Yoon, A. Heller and C. B. Mullins, *ACS Nano*, 2018, **12**, 12912–12922.
155 S. Feng, Y. Lu, X. Lu, H. Chen, X. Wu, M. Wu, F. Xu and Z. Wen, *Adv. Energy Mater.*, 2024, **14**, 2303773.
156 Z. Yang, J. Xie, Y. Li, Y. He, G. Liu, G. Qu, G. Zhang, Y. Wang, J. Zhou, Y. Huang and C. Wang, *J. Am. Chem. Soc.*, 2025, **147**, 44060–44071.
157 H. Chen, H. Yuan, Z. Dai, S. Feng, M. Zheng, C. Zheng, J. Jin, M. Wu, X. Wu, J. Lu, Y. Lu and Z. Wen, *Adv. Mater.*, 2025, **36**, 2401052.
158 L. Bai, Y. Xu, Y. Liu, D. Zhang, S. Zhang, W. Yang, Z. Chang and H. Zhou, *Nat. Commun.*, 2025, **16**, 3484.
159 C. Zhao, C. Wang, X. Liu, I. Hwang, T. Li, X. Zhou, J. Diao, J. Deng, Y. Qin, Z. Yang, G. Wang, W. Xu, C. Sun, L. Wu, W. Cha, I. Robinson, R. Harder, Y. Jiang, T. Bicer, J.-T. Li, W. Lu, L. Li, Y. Liu, S.-G. Sun, G.-L. Xu and K. Amine, *Nat. Energy*, 2024, **9**, 345–356.
160 C. Guo, X. Y. Fan, M. Liu, S. W. Xu, G. X. Wei, Z. B. Chen, Z. K. Guan, Y. Xiao, H. Xin and P. F. Wang, *Carbon Energy*, 2025, DOI: 10.1002/cey2.70037.
161 D. Yang, C. Liu, X. W. Gao, Z. Zhao, Q. Gu, Y. Long, Q. Lai, H. Chen, Z. Liu and W. B. Luo, *Angew. Chem., Int. Ed.*, 2025, **64**, e202500939.
162 J. Li, H. Hu, J. Wang and Y. Xiao, *Carbon Neutralization*, 2022, **1**, 96–116.
163 M. Hassan, Y. Zhao, Q. Liu, W. He, S. A. Riza, D. Mu, L. Li, R. Chen and F. Wu, *Carbon Neutralization*, 2025, **4**, e70000.